

1 Influence of 31 August – 1 September, 2019 ionospheric storm on HF 2 radio wave propagation

3 Yiyang Luo¹, Leonid Chernogor², Kostiantyn Garmash², Qiang Guo³, Victor Rozumenko², Yu Zheng⁴

4 ¹Department of Theoretical Radio Physics, V. N. Karazin Kharkiv National University, Kharkiv, 61022, Ukraine

5 ²Department of Space Radio Physics, V. N. Karazin Kharkiv National University, Kharkiv, 61022, Ukraine

6 ³Harbin Engineering University, 145 Nantong Street, Nangang District, Harbin, 150001, China

7 ⁴Qingdao University, 308 Ningxia Road, Qingdao, 266071, China

8 *Correspondence to:* Yu Zheng (zhengyu@qdu.edu.cn)

9 **Abstract.** The concept that geospace storms are comprised of synergistically coupled magnetic storms, ionospheric storms,
10 atmospheric storms, and storms in the electric field originating in the magnetosphere, the ionosphere and the atmosphere
11 (i.e., electrical storms) was validated a few decades ago. Geospace storm studies require the employment of multiple-method
12 approach to the Sun–interplanetary medium–magnetosphere–ionosphere–atmosphere–Earth system. This study provides
13 general analysis of the 30 August–2 September 2019 geospace storm, the analysis of disturbances in the geomagnetic field
14 and in the ionosphere, as well as the influence of the ionospheric storm on the characteristics of HF radio waves over the
15 People's Republic of China. One of the interesting features of this geospace storm is its duration, of up to four days. The
16 main results of the study are as follows. The energy and power of the geospace storm have been estimated to be 1.5×10^{15} J
17 and 1.5×10^{10} W, and thus this storm is weak. The energy and power of the magnetic storm have been estimated to be
18 1.5×10^{15} J and 9×10^9 W, i.e., this storm is moderate, and a characteristic feature of this storm is the duration of the main
19 phase, of up to two days. The recovery phase also was lengthy, no less than two days. On 31 August 2019 and on 1
20 September 2019, the variations in the H and D components attained 60–70 nT, while the Z -component variations did not
21 exceed 20 nT. On 31 August 2019 and on 1 September 2019, the level of fluctuations in the geomagnetic field in the 100–
22 1000 s period range increased from 0.2–0.3 nT to 2–4 nT, while the energy of the oscillations showed a maximum in the
23 300–400 s to 700–900 s period range. The geospace storm was accompanied by a moderate to strong negative ionospheric
24 storm. During 31 August 2019 and 1 September 2019, the electron density in the ionospheric F region reduced by a factor of
25 1.4 to 2.4 times as compared to the values on the reference day. The geospace storm gave rise to appreciable disturbances
26 also in the ionospheric E region, as well as in the E_s layer. In the course of the ionospheric storm, the altitude of reflection of
27 radiowaves could sharply increase from ~150 km to ~300–310 km. The geospace storm was accompanied by the generation
28 of atmospheric gravity waves modulating the ionospheric electron density. For the ~30 min period oscillation, the amplitude
29 of the electron density disturbances could attain ~40 %, while it did not exceed 6 % for the ~15 min period. The results
30 obtained have made a contribution to understanding of the geospace storm physics, to developing theoretical and empirical
31 models of geospace storms, to the acquisition of detailed understanding of the adverse effects that geospace storms have on
32 radiowave propagation and to applying that knowledge to effective forecasting these adverse influences.

33 1 Introduction

34 Geospace storms are comprised of synergistically coupled magnetic storms, ionospheric storms, atmospheric storms, and
35 storms in the electric fields originating in the magnetosphere, the ionosphere, and the atmosphere (i.e., electrical storms)
36 (Chernogor and Rozumenko, 2008; Chernogor, 2011; Chernogor and Domnin, 2014). Consequently, the discussion of only
37 one of the storms would be incomplete, and therefore, the analysis of geospace storms requires the employment of a systems
38 approach. These storms are of solar origin, and they may be accompanied by solar flares, coronal mass ejections, high speed
39 solar wind streams, energetic proton fluxes, and solar radio bursts. All listed above processes affect the magnetosphere, the

40 ionosphere, the atmosphere, and the internal terrestrial layers through the interplanetary medium. Their joint study requires
41 clustered-instrument studies of the internal layers in the Sun–interplanetary-medium–magnetosphere–ionosphere–
42 atmosphere–Earth (SIMMIAE) system (Chernogor and Rozumenko, 2008; Zalyubovsky et al., 2008; Chernogor, 2011;
43 Chernogor and Domnin, 2014; Chernogor and Rozumenko, 2011, 2012, 2014, 2016, 2018; Chernogor et al., 2020). The
44 study of geospace storms, which are not quite correctly termed by some authors as the magnetic storms, the ionospheric
45 storms, or thermospheric storms, has almost a 100 year history. The proper magnetic storms have been observed for about
46 400 years. The results of the first observations of ionospheric disturbances occurring during magnetic storms were described
47 by Hafstad and Tuve (1929) and Appleton and Ingram (1935).

48 Matsushita (1959) was the first to apply statistics to ionospheric storms. Later, the statistical approach was
49 employed by Chernogor and Domnin (2014). The statistics of magnetic and ionospheric storms is presented in (Vijaya
50 Lekshmi et al., 2011; Yakovchouk et al., 2012; Zolotukhina et al., 2018).

51 A few authors (Danilov and Morozova, 1985; Pröls, 1995, 1997; Laštovička, 1996; Fuller-Rowell et al., 1997;
52 Buonsanto, 1999; Danilov and Laštovička, 2001; Danilov, 2013) generalized the observations of ionospheric storms.

53 The results of recent studies of ionospheric storm effects are presented in a large number of papers (see, e.g., Blanch
54 et al., 2005; Mendillo, 2006; Pirog et al., 2006; Pröls, 2006; Kamide and Maltsev, 2007; Borries et al., 2015; Liu et al.,
55 2016; Polekh et al., 2017; Shpynev et al., 2018; Stepanov et al., 2018; Yamauchi et al., 2018; Blagoveshchensky and
56 Sergeeva, 2019; Chernogor et al., 2020; Mosna et al., 2020).

57 Many authors have employed the systems approach to the SIMMIAE system over the last 40 years. The basics of
58 the systems paradigm are stated and validated by Chernogor and Rozumenko [2008, 2011, 2012, 2014, 2016, 2018],
59 Chernogor [2011], and Chernogor and Domnin [2014].

60 The study of geospace storms is of major scientific importance (Gonzalez et al., 1994; Knipp and Emery, 1998,
61 Freeman, 2001; Space..., 2001; Benestad, 2002; Carlowicz and Lopez, 2002; Lathuillère et al., 2002; Feldstein et al., 2003;
62 Bothmer and Daglis, 2006; Lilensten and Bornarel, 2006). Mechanisms for subsystem coupling, both positive and negative
63 ones, in the SIMMIAE system, as well as feedback and precondition of the system components have not been sufficiently
64 well studied. In particular, Gonzalez et al. (1994) made an excellent review summarizing information on geomagnetic storms
65 up to the early 1990s. Since then, the understanding of geomagnetic storms has significantly advanced [Danilov, 2013]. The
66 authors have used the relation given by Gonzalez et al. (1994) for the magnetic storm energy. Knipp and Emery (1998)
67 described in detail the processes accompanying the November 2–11, 1993 geomagnetic storm. Feldstein et al. (2003)
68 analyzed in detail the energy of the processes acting in the magnetosphere during two particular storms.

69 The dynamics of the processes, energy transfer, the appearance of trigger mechanisms for energy release, etc.,
70 remain not fully understood.

71 The study of geospace storms is also of special interest to estimate serious malfunctions in numerous systems:
72 radar, telecommunications, radionavigation, radio astronomy, and in ground-based power system, etc. (Goodman, 2005).
73 Storms have the potential to harm humans on the ground or in the near-Earth space environment. Modern society and human
74 well-being become reliant more and more on space-based technologies, and consequently, on the state of space weather and
75 geospace storms. The manifestations of geospace storms vary over the solar cycle, and depend on season, local time,
76 latitude, longitude, and so on. Therefore, there is an urgent need to study each sufficiently large geospace storm. Such an
77 investigation reveals both general storm properties and its specific features.

78 The purpose of this paper is to present a general analysis of the 30 August–2 September, 2019 geospace storm, to
79 analyze disturbances in the ionosphere and in the geomagnetic field, and to examine the influence of the ionospheric storm
80 on the characteristics of the HF radio wave propagating over the People's Republic of China area. One of the interesting
81 features of this geospace storm is its duration, of up to four days.

82 In this paper, a brief description of the instrumentation and the techniques employed is presented first. This is
83 followed by a general analysis of the space weather state, the magnetic and ionospheric storms. Next, a description of the
84 results of radio observations obtained at oblique incidence on the reference day and in the course of the geomagnetic storm is
85 examined in detail. Finally, the results of analysis of the geomagnetic storm features are discussed, and the main results are
86 listed.

87 2 Instrumentation and measurement techniques

88 2.1 Observational instruments

89 *Fluxmeter magnetometer.* The magnetometer is located at the Kharkiv V. N. Karazin National University Magnetometer
90 Observatory (49.64°N, 36.93°E). It acquires data on variations in the horizontal (H , D) geomagnetic field components in the
91 1–1000 s period range with a 0.5 s temporal resolution delivering 1 pT–1 nT sensitivity. The fluxmeter magnetometer is
92 described in detail by Chernogor (2014) and Chernogor and Domnin (2014).

93 *Three-Axis Fluxgate Magnetometer.* The LEMI-017 Meteomagnetic Station (49.93°N, 36.95°E) is located at the
94 Institute of Radio Astronomy of NASU Low Frequency Observatory (49.93°N, 36.95°E) [Magnetic field variations
95 <http://geospace.com.ua/en/observatory/metmag.html>, last access: 15 June 2020]. It takes measurements of the geomagnetic
96 field H , D , and Z components at 1 s interval with 10 pT sensitivity.

97 *Multi-frequency multipath system involving the software-defined radio for the oblique incidence radio sounding of*
98 *the ionosphere.* It is located at the Harbin Engineering University campus, the People's Republic of China (45.78°N,
99 126.68°E) (Chernogor et al., 2019a, b, c, 2020; Guo et al., 2019a, b, c, 2020; Luo et al., 2020a). The ionosphere is
100 continuously monitored over eleven radio paths utilizing emissions from broadcasting stations in the 5–10 MHz frequency
101 range and located in Japan, the Russian Federation, Mongolia, the Republic of Korea, and the People's Republic of China
102 (Fig. 1), the radio path lengths (Table 1) are found in the $(1-2) \times 10^3$ km distance range, and the signal reception and
103 processing is performed at the Harbin Engineering University.

104 *Ionosondes.* They are used to assess a general state of the ionosphere. The WK546 URSI code ionosonde at the City
105 Wakkanai (45.16°N, 141.75°E), Japan, is the closest to Harbin (Ionosonde Stations in
106 Japan: URL: wdc.nict.go.jp/IONO/HP2009/contents/Ionosonde_Map_E.html, last access: 15 June 2020). To assess the
107 characteristic extent of the ionospheric storm, the City of Moscow (the Russian Federation) ionosonde data are used (List of
108 years for MOSCOW: <https://lgdc.uml.edu/common/DIDBYearListForStation?ursiCode=MO155>, last access: 15 June 2020).

109 2.2 Analysis techniques

110 The fluxmeter magnetometer data recorded initially on a relative scale have been converted into absolute values using the
111 magnetometer transfer function. Then, temporal dependencies of the geomagnetic field have been subjected to the systems



Figure 1: Layout of the propagation paths used for monitoring dynamic processes acting in the ionosphere.

112 spectral analysis, which employs simultaneously the short-time Fourier transform, the wavelet transform using the Morlet
 113 wavelet as a basis function, and the Fourier transform in a sliding window with a width adjusted to be equal to a fixed number
 114 of harmonic periods (Chernogor, 2008). Analysis of the obtained spectra follows.

Table 1

Basic parameters of 11 radio paths used for probing the ionosphere at oblique incidence. Retrieved from <https://fmscan.org/index.php>

Transmitter			Propagation path midpoint			
Frequency [kHz]	North latitude [deg.]	East longitude [deg.]	Location [country]	Distance to Harbin [km]	North latitude [deg.]	East longitude [deg.]
5,000	34.95	109.56	Lintong/ Pucheng (China)	938	40.37	118.12
6,015	37.21	126.78	Hwaseong (ROK)	475	41.50	126.73
6,055	35.47	140.21	Chiba/ Nagara (Japan)	805	40.63	133.45
6,175	39.75	116.81	Beijing (China)	525	42.77	121.75
6,600	37.60	126.85	Goyang (ROK)	455	41.69	126.77
7,260	47.80	107.17	Ulaanbaatar/ Khonkhor (Mongolia)	748	46.79	116.93
7,345	62.24	129.81	Yakutsk (Russia)	923	54.01	128.25
9,500	38.47	114.13	Shijiazhuang (China)	655	42.13	120.41
9,520	40.72	111.55	Hohhot (China)	670	43.25	119.12
9,750	36.17	139.82	Yamata (Japan)	785	40.98	133.25
9,830	39.75	116.81	Beijing (China)	525	42.77	121.75

115 The Radio Astronomy of the National Academy of Sciences of Ukraine three-axis fluxgate magnetometer has been
 116 used to control a general state of the geomagnetic field, and a specific signal processing procedure was not needed.

117 The data acquired by the multi-frequency multipath system for the oblique incidence radio sounding of the
 118 ionosphere have been subjected to processing in detail, and the products included the universal time dependencies of the
 119 Doppler spectra, the main ray amplitude, $A(t)$, and the Doppler shift of frequency, $f_D(t)$. Further, the $f_D(t)$ and $A(t)$ were
 120 subjected to secondary processing to obtain the trends $\bar{f}_D(t)$ and $\bar{A}(t)$, the fluctuations $\delta f_D(t) = f_D(t) - \bar{f}_D(t)$,
 121 $\delta A(t) = A(t) - \bar{A}(t)$, and the spectra in the period range $T \approx 1-60$ min and greater (Chernogor, 2008).

122 3 Analysis of the space weather state

123 The space weather variations under study are the event of CIR/CH HS origin combined with solar sector boundary crossing
124 event, which could affect geomagnetic situation (see <ftp://ftp.swpc.noaa.gov/pub/warehouse/2019/WeeklyPDF/prf2296.pdf>;
125 Koskinen, 2011). The data retrieved from <https://omniweb.gsfc.nasa.gov/form/dx1.html> have been used to analyze the solar
126 wind parameters. On 29 August 2019, the proton density, n_{sw} , exhibited an increase from $\sim 10^6 \text{ m}^{-3}$ to $15 \times 10^6 \text{ m}^{-3}$, and
127 subsequently, a decrease from $15 \times 10^6 \text{ m}^{-3}$ to $1 \times 10^6 \text{ m}^{-3}$ in the course of the next three days (Fig. 2). In the course of 28 and
128 29 August 2019 and of the first half of 30 August 2019, the solar wind bulk speed, V_{sw} , varied from $\sim 350 \text{ km s}^{-1}$ to 500 km s^{-1} .
129 After 12:00 UT on 30 August 2019 through about 01:00 UT on 1 September 2019, the V_{sw} value exhibited an increase
130 from $\sim 400 \text{ km s}^{-1}$ to 750 km s^{-1} with a peak of 835 km/s observed early on 1 September 2019 (see
131 <ftp://ftp.swpc.noaa.gov/pub/warehouse/2019/WeeklyPDF/prf2296.pdf>). During almost four days, $V_{sw} \approx 600\text{--}750 \text{ km s}^{-1}$.
132 Before 12:00 UT on 30 August 2019, the temperature, T_{sw} , of the solar wind particles was observed to be in the $(1\text{--}$
133 $2) \times 10^5 \text{ K}$ range. After 12:00 UT on 30 August 2019, it showed an increase from 10^5 K to $4.4 \times 10^5 \text{ K}$ in the course of 24 h,
134 and eventually, fluctuating, it exhibited a gradual decrease from $4.4 \times 10^5 \text{ K}$ to 10^5 K . As expected, the increases in n_{sw} and
135 V_{sw} gave rise to an increase in the solar wind dynamic pressure, from $\sim 0.2 \text{ nPa}$ to $\sim 3 \text{ nPa}$. The East–West B_y and the North–
136 South B_z components of the interplanetary magnetic field exhibited fluctuations in the -3 nT to 8 nT and from -7 to 3 nT
137 ranges, respectively. Since approximately 12:00 UT on 30 August 2019, the value of the B_z component remained
138 predominantly negative. This indicated that the magnetic storm ensued. Over the following day (from 08:00 UT on 30
139 August 2019 to 07:00 UT on 3 September 2019), energy input per unit time, ϵ_A , from the solar wind into the Earth's
140 magnetosphere occasionally increased to $14\text{--}15 \text{ GJ s}^{-1}$; before the storm commencement, the ϵ_A value did not exceeded 1 GJ
141 s^{-1} .

142 The K_p index values exhibited variations from 0 to 2 before the storm commencement, and from ~ 2 to 5.7 over four
143 days afterwards. Before the storm commencement, the D_{st} index was observed to fluctuate in the -10 nT to 6 nT range. At
144 about approximately 12:00 UT on 30 August 2019, $D_{st} \approx 12 \text{ nT}$; from 10:00 UT to 14:00 UT, the storm commencement was
145 observed to occur. After 20:00 UT on 30 August 2019, the D_{st} values began to show a gradual decrease to -55 nT , which
146 was attained at about 06:00 UT on 1 September 2019; over this time period, the storm main phase was observed to occur.
147 After 06:00 UT on 1 September 2019, the storm transitioned to the recovery phase, which lasted for a few days. Thus, this
148 magnetic storm was seen to be of quite a long duration over the last few years, but it was not the strongest, which is its main
149 feature. A long duration ionospheric storm was expected to follow the longest duration magnetic storm. The geomagnetic
150 and ionospheric storm features are described further in detail.

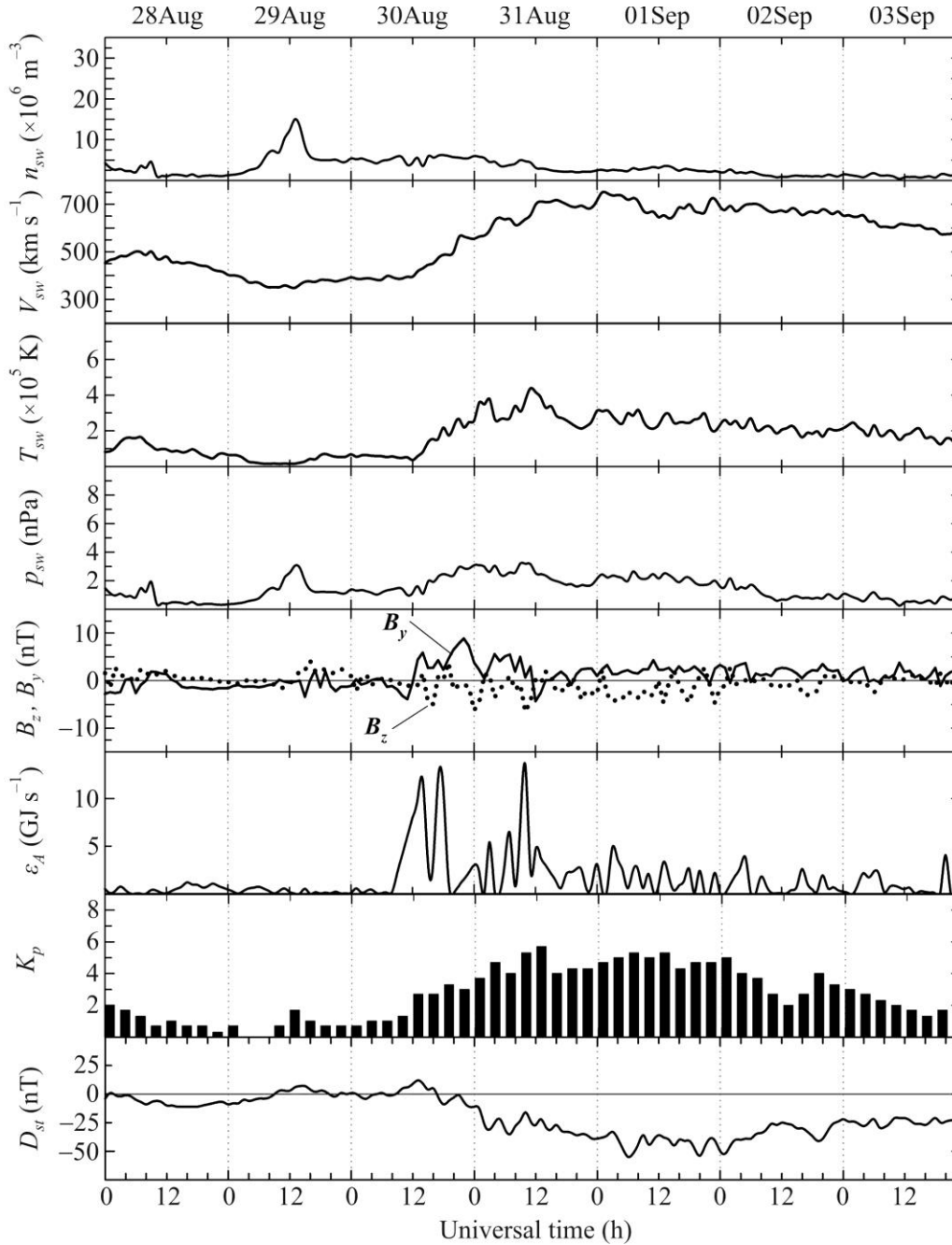
151 4 Analysis of the magnetic storm

152 4.1 Level of geomagnetic field variations

153 Magnetic measurements at the Institute of Radio Astronomy of NASU Low Frequency Observatory, Ukraine (49.93° N ,
154 36.95° E) show that the state of the geomagnetic field was quiet on 29 August 2019 (panel (a) in Fig. 3). After 12:00 UT on
155 30 August 2019, relatively small, $\sim 10\text{--}20 \text{ nT}$, variations appeared in all geomagnetic field components (see panel (b) in
156 Fig. 3). On 31 August 2019, the variations increased up to $60\text{--}70 \text{ nT}$ (see panel (c) in Fig. 3). The Z component was
157 changing less, no more than by 20 nT . The variations on 1 September 2019 remained approximately the same (see panel (d)
158 in Fig. 3). The fluctuation excursions of the components significantly decreased on 2 September 2019 (see panel (e) in
159 Fig. 3). In the course of the next two days, the magnetic field remained weakly disturbed (see panel (f) in Fig. 3); the
160 fluctuation excursions did not exceed 15 nT (see panel (f) in Fig. 3).

161 **4.2 Level of geomagnetic field fluctuations**

162 Up to 11:00 UT on 29 August 2019, the variations in the geomagnetic field H and D components in the 1–1000 s period
 163 range at the V. N. Karazin Kharkiv National University Geomagnetic Observatory, Ukraine (49.65°N, 36.93°E) were
 164 insignificant, less than 0.2–0.3 nT (Fig. 4); from 11:00 UT to 17:00 UT, their level occasionally showed increases of up to
 165 ± 1 nT. On 30 August 2019, approximately in the course of the sudden storm commencement, the level of fluctuations
 166 exhibited an increase by a factor of 2 to 3 times, which persisted for about 4–5 h. On 31 August 2019, in the course of the
 167



168
 169 Figure 2: Universal time dependencies of the solar wind parameters: proton number density n_{sw} , temperature T_{sw} , plasma
 170 flow speed V_{sw} (retrieved from <https://omniweb.gsfc.nasa.gov/form/dx1.html>), calculated dynamic pressure p_{sw} , components
 171 B_z and B_y of the interplanetary magnetic fields (retrieved from <https://omniweb.gsfc.nasa.gov/form/dx1.html>), calculated
 172 energy input per unit time, ϵ_A , from the solar wind into the Earth's magnetosphere; K_p - and D_{st} -index (retrieved from
 173 <https://omniweb.gsfc.nasa.gov/form/dx1.html>) for 28 August–3 September 2019 period. Dates are shown along the upper
 174 abscissa axis.

175

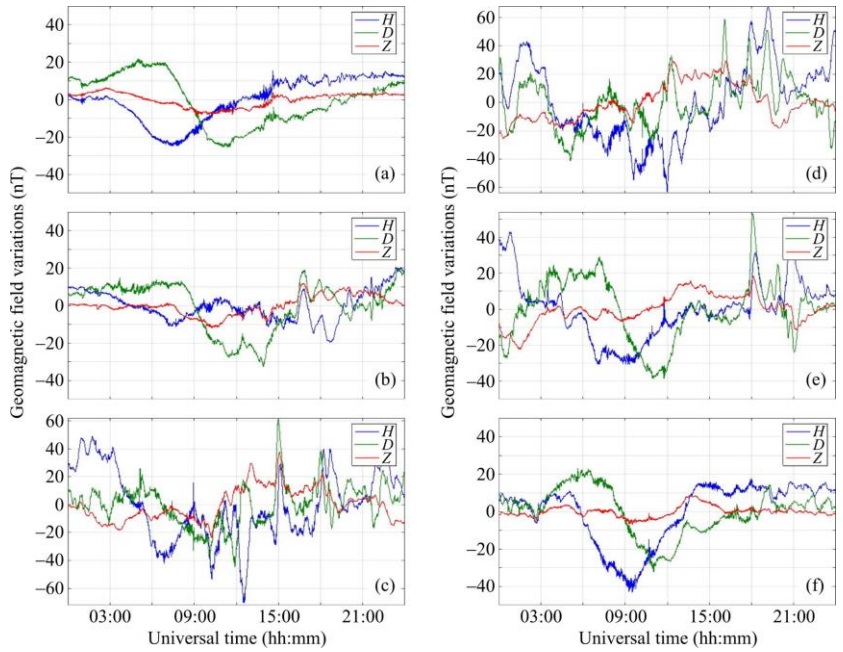


Figure 3: H , D , Z components for (a) 29 August 2019; (b) 30 August 2019; (c) 31 August 2019; (d) September 01, 2019; (e) September 02, 2019; (f) September 03, 2019 (retrieved from

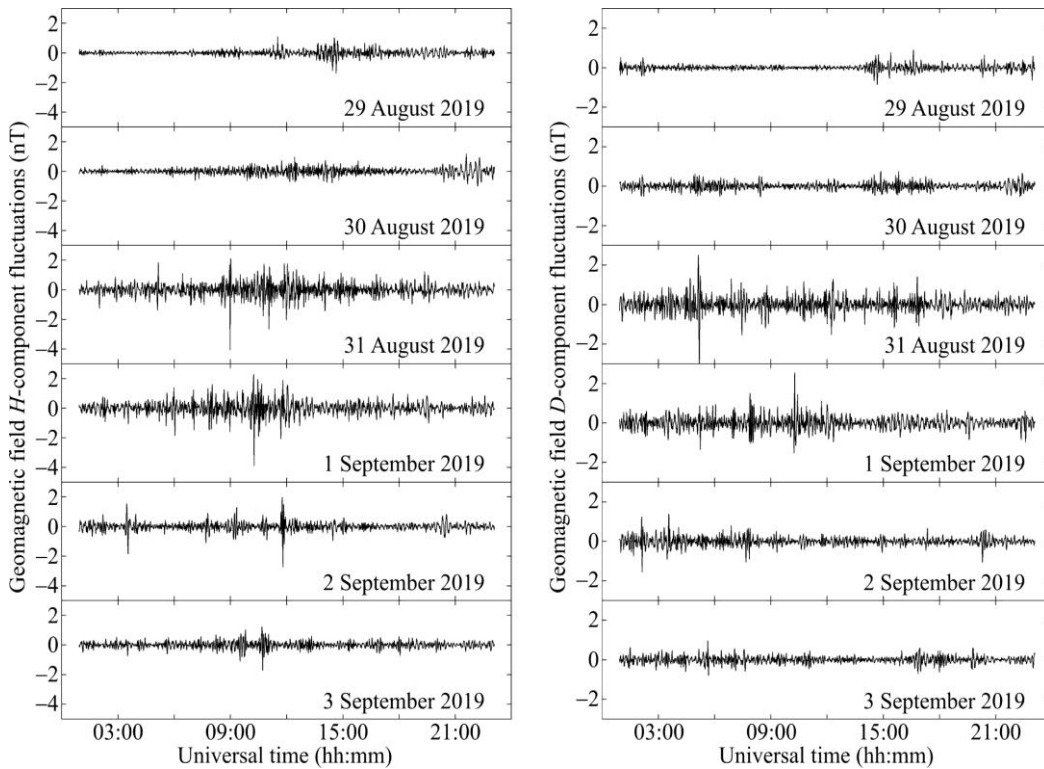


Figure 4: Magnetic field variations at V. N. Karazin Kharkiv National University Magnetometer Observatory.

179 storm main phase, the level of fluctuations showed an increase of up to 1.5–2 nT, and occasionally even of up to 4 nT. The
180 duration of this effect was no less than 10 h.

181 On 1 September 2019, approximately from 08:00 UT to 13:00 UT, a considerable, of up to 2–4 nT, increase in the
182 level of fluctuations was also observed to occur. On 2 and 3 September 2019, the level of fluctuations also exhibited
183 occasional enhancements, of up to 1.5–2 nT, approximately 1 h in duration.

184 **5 Analysis of ionospheric state**

185 The state of the ionosphere has been analyzed in general using the data from two ionosondes. The first of these is located in
186 the vicinity of the propagation paths used for obliquely sounding the ionosphere, viz, near the City Wakkanai (45.16°N,
187 141.25°E), Japan. To assess the characteristic extent of the ionospheric storm, ionosonde data from the City of Moscow
188 (55.47°N, 37.30°E), the Russian Federation, have been used.

189 **5.1 Data from ionosonde in Japan**

190 Since 29 August 2019 to 3 September 2019, the minimum frequency, f_{\min} , showed insignificant variations, from 1.4 MHz to
191 1.5 MHz. Only on 1 September 2019, the f_{\min} was observed to exhibit spikes of up to 1.7–2 MHz.

192 The behavior of the E -layer critical frequency, $f_{oE}(t)$, was observed to be approximately the same on all the days.
193 During the daytime, this frequency attained 2.9–3.2 MHz; in the local evening, it decreased to 1.8 MHz; during night, the f_{oE}
194 was not observed, and in the course of three hours in the morning, it showed an increase from 1.8 MHz to ~3 MHz.

195 The sporadic- E critical frequency, f_{oE_s} , exhibited variations in a broad range of frequencies, from ~3 MHz to ~12–
196 16 MHz. In the course of the storm's main phase, the f_{oE_s} variations were insignificant.

197 Variations in the critical frequency, $f_oF_2(t)$, of the F_2 layer for the ordinary wave were observed to be small. During
198 the daytime, this frequency was observed to be approximately 5 MHz, and during night, it showed a gradual decrease from
199 4 MHz to 3 MHz.

200 Generally, the universal time variations in the virtual height, $h'_E(t)$, of the E layer were observed to be
201 insignificant, a mere 5–10 km. However, approximately from 16:00 UT to 19:00 UT on 31 August 2019 and on 1 September
202 2019, the height $h'_E(t)$ showed an increase from ~100 km to ~120 km.

203 The sporadic E_s layer virtual height exhibited considerable fluctuations, from ~80 km to 160–170 km.

204 We have not succeeded in obtaining reliable data on the virtual height, $h'_{F_2}(t)$, of the F_2 layer. Most likely, it varied
205 from 200 km to 300 km.

206 **5.2 Data from ionosonde at Moscow**

207 The minimum frequency, f_{\min} , values most frequently occurred in the 1.2–1.7 MHz range, and spikes of up to 2–3 MHz were
208 observed only sometimes. From 07:30 UT to 08:30 UT on 31 August 2019, the f_{\min} showed an increase from 1.4 MHz to
209 2.2–2.4 MHz. During 1 through 3 September 2019, the f_{\min} values exhibited considerable fluctuations.

210 The E -layer critical frequency, $f_{oE}(t)$, tracked the local time dependence of the electron density. The root-mean-
211 square f_{oE} deviation did not exceed ~0.1 MHz. In the daytime, the f_{oE} attained approximately 3 MHz, in the morning and in
212 the evening, it showed an increase or a decrease of 1.3–1.4 MHz. Under nighttime conditions, we have not succeeded in
213 measuring f_{oE} .

214 The sporadic- E critical frequency, f_{oE_s} , exhibited considerable fluctuations, from 2 MHz to 5–7 MHz. The
215 fluctuation excursions in f_{oE_s} under daytime conditions were observed to be greater than under nighttime conditions.

216 On 31 August 2019, from 05:00 UT to 08:00 UT, the f_{oE_s} exhibited an increase from 3 MHz to 6–7 MHz.

217 The critical frequency, $f_oF_2(t)$, of the F_2 layer for the ordinary wave showed a decrease to 3 MHz during the 28/29
218 August 2019 night, which was followed by an increase to 4.5 MHz during the daytime, and even by an increase up to 5 MHz
219 on 30 August 2019. During almost all local daytime on 31 August 2019, the $f_oF_2(t)$ was observed to be 0.7–1.1 MHz lower
220 than on 29 August 2019. On 31 August 2019, from 09:00 UT to 11:00 UT and from 12:00 UT to 15:00 UT, an increase in
221 $f_oF_2(t)$ was observed to be 0.7–0.8 MHz. During night and in the morning on 1 September 2019, the f_oF_2 values were
222 observed to be 0.5–0.6 MHz lower than those observed on 2 September 2019; during the daytime, the difference between
223 these frequencies did not exceeded 0.2–0.3 MHz on average.

224 The virtual height, h'_E , of the E layer exhibited fluctuations in the 95–100 km range. On 31 August 2019, from
225 10:00 UT to 13:00 UT, it showed an increase from 102 km to 113 km. A considerable increase in h'_E from 110 km to 133
226 km also occurred at ~12:30 UT on September 1, 2019.

227 The sporadic E_s layer virtual height, h'_{Es} , exhibited fluctuations in the 100–105 km to 130–140 km range. On 31
228 August 2019, from 10:00 UT to 13:00 UT, this height showed an increase from ~105 km to 130 km. An increase from ~110
229 km to 125–132 km also took place on 1 September 2019, from 08:00 UT to 14:00 UT.

230 The virtual height, h'_{F_2} , of the F_2 layer exhibited significant, from ~200 km to 400–500 km, fluctuations during the
231 29 August to 3 September 2019 period. Sharp, from 250 km to 400–450 km, spikes in h'_{F_2} took place on 31 August 2019,
232 during 13:30–14:30 UT and 16:00–16:30 UT periods. Considerable, from 250–300 km to 400–500 km, variations in h'_{F_2}
233 were also observed to occur during the 31 August 2019 to 1 September 2019 night, as well as from 16:00 to 18:00 UT on 1
234 September 2019.

235 **6 Ionosphere: Oblique incidence sounding**

236 **6.1 Lintong/Pucheng to Harbin radiowave propagation path**

237 The radio station operating at 5,000 kHz is located in the People's Republic of China at a great-circle propagation path range,
238 R , of 1,875 km from the receiver.

239 Approximately from 00:00 UT to 07:00 UT on 29 August 2019, i.e., during sunlit hours on the reference day, the
240 signal amplitude, A , was observed to be ~–70 dBV, and the Doppler shift of frequency in the main ray signal, $f_D(t)$, to be
241 ~0.0 Hz, as can be seen in Fig. 5. After sunset at ~07:00 UT, i.e., in the evening hours, the A showed a gradual increase of
242 up to –40 dBV. The $f_D(t)$ values gradually decreased from 0 Hz to –(0.5–1) Hz. Approximately from 09:00 UT to 16:00 UT,
243 the Doppler spectra were observed to significantly broaden, from –2.5 Hz to 2 Hz. On 30 August 2019, the $f_D(t)$ exhibited
244 considerable, from –0.3 Hz to 0.4 Hz, variations during the 18:00 UT to 22:00 UT period.

245 On 31 August 2019, the $f_D(t)$ changed from –0.3 Hz to 0.3 Hz over the 12:00–18:00 UT period when quasi-periodic
246 variations in the $f_D(t)$ took place with ~40 min period, T , and ~0.20–0.25 Hz amplitude, f_{Da} . From 17:00 UT to 22:00 UT, the
247 amplitude $A(t)$ exhibited considerable, up to 15–20 dBV, variations.

248 On 1 September 2019, the $f_D(t)$ showed significant increase, from –1.8 Hz to 1.4 Hz, in the course of sunset in the
249 ionosphere. The ionospheric storm effect was observed to occur from at least 10:00 UT to 19:00 UT. The amplitude $A(t)$ was
250 observed to exhibit considerable, up to 20 dBV, variations during the 11:30–21:00 UT period. On 2 and 3 September 2019,
251 the behavior of the Doppler spectra almost did not differ from that on the undisturbed day.

252 **6.2 Hwaseong to Harbin radiowave propagation path**

253 The 6,015 kHz transmitter is located in the Republic of Korea at an ~950 km distance from the receiver, and it did not
254 operate from 00:00 UT to 03:40 UT.

255

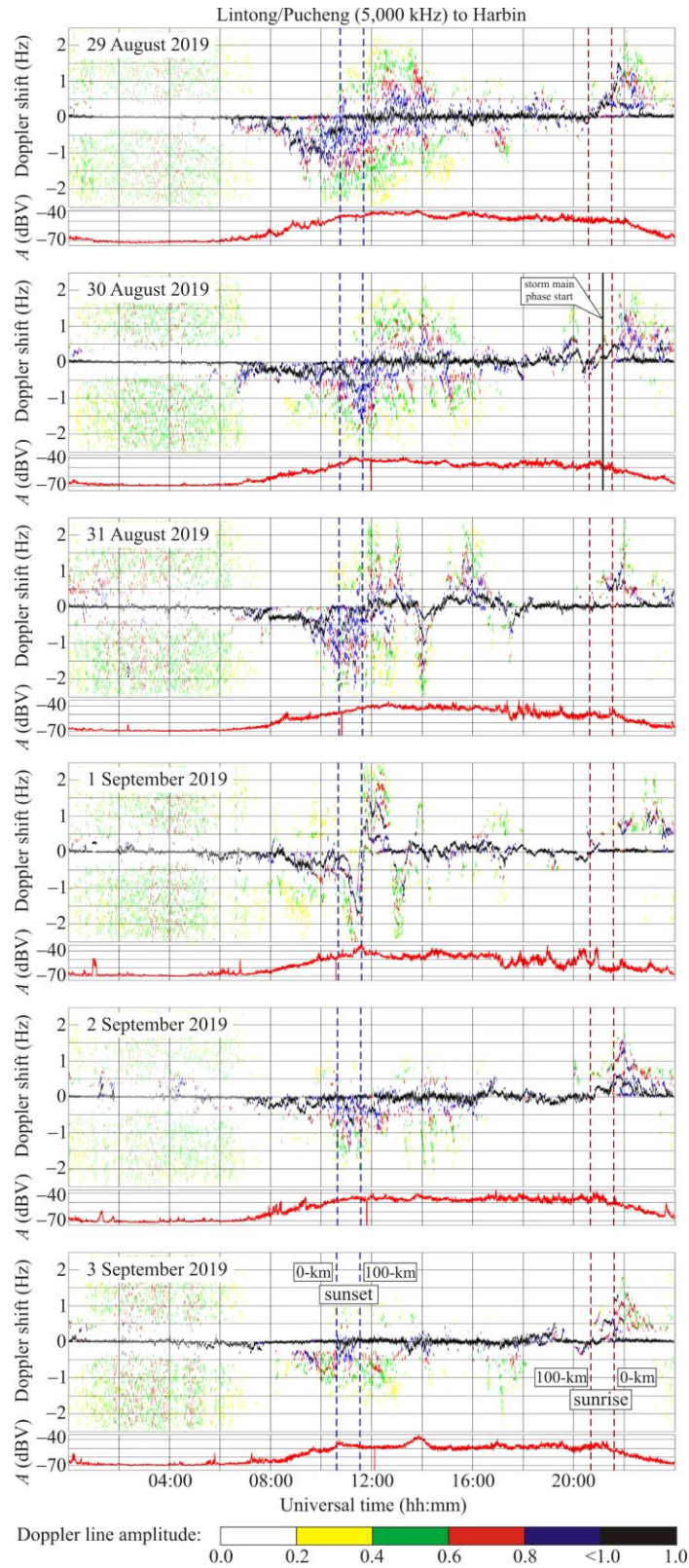


Figure 5: Universal time variations of Doppler spectra and relative signal amplitude, A , along the Lintong/Pucheng to Harbin propagation path for 29–31 August 2019 and 1–3 September 2019 (panels from top to bottom). The Doppler shift plot is comprised of 117,600 samples in every 1 h interval. The signal amplitude, A , at the receiver output in decibels, dBV, relative to 1 V is shown below the Doppler spectrum in every panel. The dashed lines indicate the sunsets and sunrises at 0- and 100-km altitude.

258 On 29 August 2019, the Doppler shift of frequency $f_D(t) \approx 0$ Hz at almost all times (Fig. 6). The spectra were
259 observed to exhibit maximum broadening near the dawn and dusk terminators. The variations in the signal amplitude
260 represented the local time behavior.

261 On 30 August 2019, considerable (from -0.4 Hz to 0.4 Hz) variations in the Doppler shift of frequency in the main
262 ray were observed to occur from 13:00 UT to 21:00 UT with an ~ 70 – 110 min quasi-period, T , and an ~ 0.4 Hz amplitude, f_{Da} .

263 On 31 August 2019, quasi-periodic changes in $f_D(t)$ were observed to occur from 12:00 UT to 17:00 UT with $T \approx 40$
264 min and $f_{Da} \approx 0.4$ – 0.7 Hz.

265 On 1 September 2019, very significant (from -1.5 Hz to 1.3 Hz) variations in $f_D(t)$ and the Doppler spectra took
266 place from 10:00 UT to 14:00 UT and from 16:30 UT to 19:00 UT. From approximately 10:00 UT to 21:00 UT, large (up to
267 30 dBV) variations in signal amplitudes were evident.

268 On 2 and 3 September 2019, the Doppler spectra and signal amplitudes did not exhibit considerable variations.

269 **6.3 Chiba/Nagara to Harbin radiowave propagation path**

270 The radio station operating at 6,055 kHz is located in Japan at an $\sim 1,610$ km range from the receiver. The signal
271 transmissions were absent from 15:00 UT to 22:00 UT.

272 The Doppler spectra exhibited similar behavior on 29, 30, and 31 August 2019 (Fig. 7). From 06:00 UT to 15:00 UT, the
273 spectra were observed to be spread; they occupied the -1.5 Hz to 1.5 Hz frequency range.

274 On 1 September 2019, the Doppler spectra exhibited behavior sharply different from that observed on the preceding
275 day. The spread was evident weakly; from 10:00 UT to 15:00 UT, the Doppler shifts of frequency exhibited sharp changes
276 from -1.5 Hz to 1.3 Hz; the quasi-periodic process with the ~ 60 min and greater period, T , and the ~ 0.2 Hz and greater
277 amplitude, f_{Da} , became evident. On this day, the signal amplitude also exhibited considerable (up to 20 dBV) fluctuations.

278 On 2 September 2019, the Doppler spectra remained still disturbed over the 07:00–12:00 UT period.

279 On 3 September 2019, the Doppler spectrum spread was insignificant. The Doppler shift of frequency, $f_D(t)$, was
280 observed to be close to zero level most of the time.

281 **6.4 Beijing to Harbin radiowave propagation path**

282 The 6,175 kHz transmitter is located in the People's Republic of China at approximately 1,050 km range from the receiver.
283 The transmitter operated only over the 09:00 UT to 18:00 UT and 20:20 UT to 24:00 UT periods.

284 On 29 and 30 August 2019, the Doppler spectra were characteristic of the single ray propagation; the second ray
285 appeared only sporadically (Fig. 8). The Doppler shift of frequency, $f_D(t)$, was observed to be close to zero level almost all
286 the time, and the signal amplitude $A(t) \approx -(30$ – $40)$ dBV.

287 On 31 August 2019, over the 12:00–18:00 UT period, the behavior of $f_D(t)$ sharply changed. The $f_D(t)$ dependence
288 became quasi-periodic with an ~ 30 min period, T , and an ~ 0.2 Hz amplitude. At approximately 14:00 UT, the f_D dependence
289 exhibited a sharp decrease from 0.2 Hz to -0.7 Hz.

290 The f_D was observed to exhibit considerable, from -1.2 Hz to 1.1 Hz, variations over the 10:00–12:00 UT and
291 16:00–18:00 UT periods on 1 September 2019, while the signal amplitude showed a decrease by 30 dBV from 16:00 UT to
292 18:00 UT.

293 On 2 and 3 September, 2019, the Doppler spectra exhibited the behavior characteristic of the quiet ionosphere.

294

295

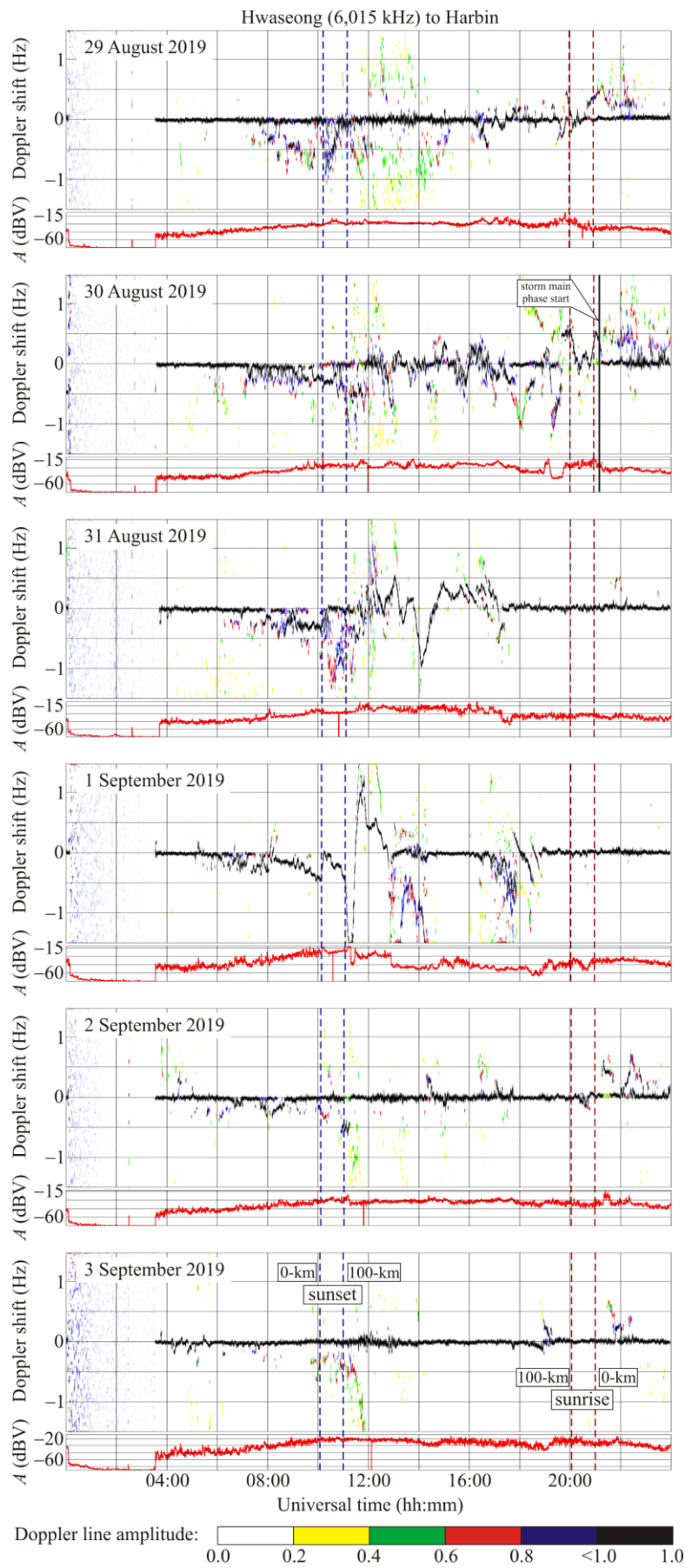


Figure 6: Same as Figure 5, but for the Hwaseong to Harbin radiowave propagation path at 6,015 kHz.

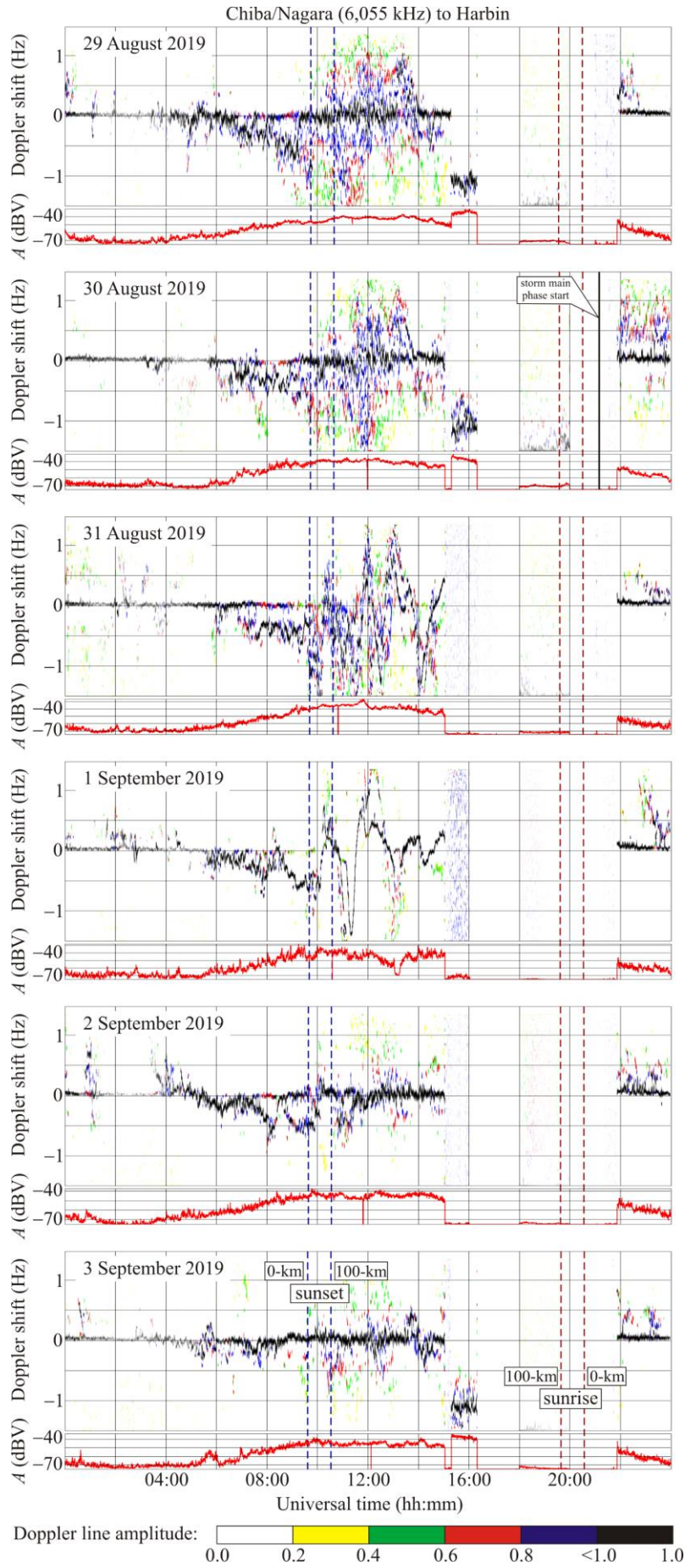


Figure 7: Same as Figure 5, but for the Chiba/Nagara to Harbin radiowave propagation path at 6,055 kHz.

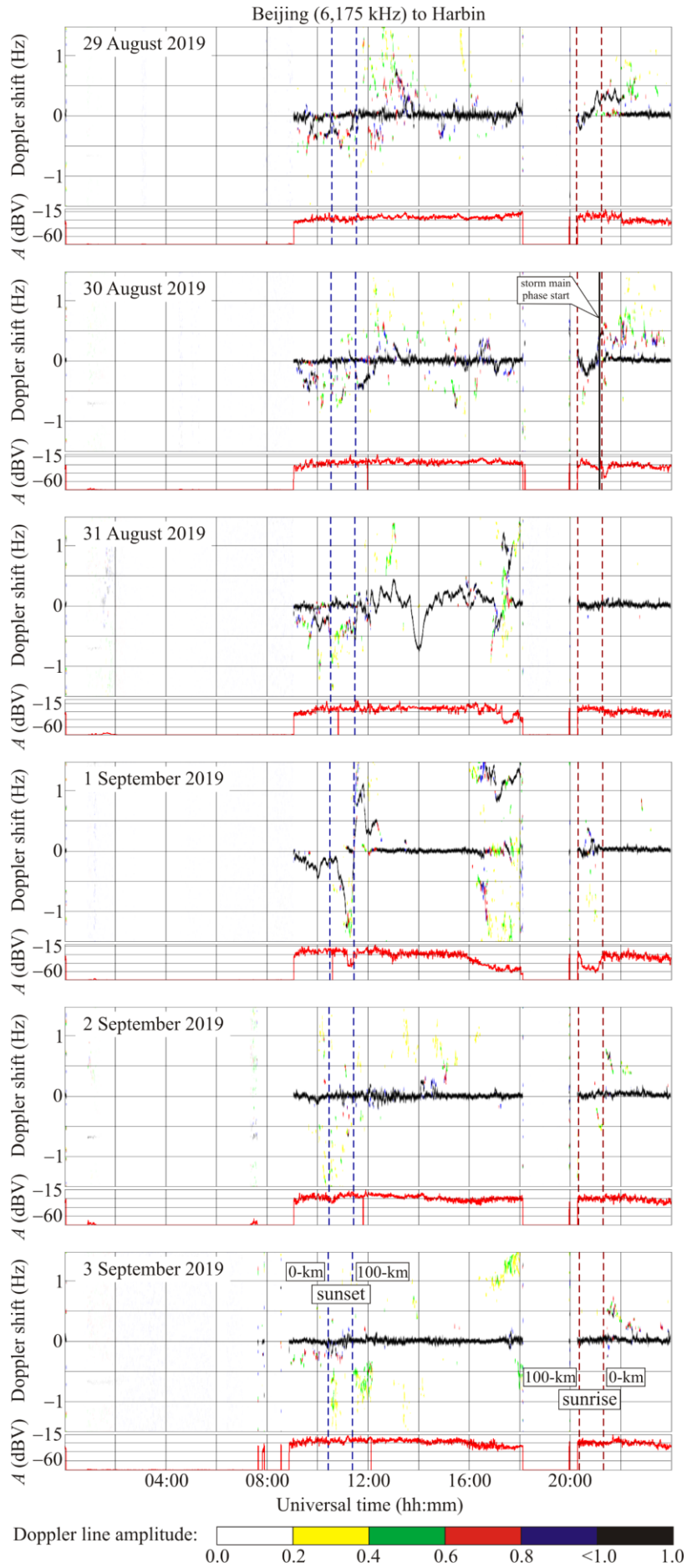


Figure 8: Same as Figure 5, but for the Beijing to Harbin radiowave propagation path at 6,175 kHz.

300 **6.5 Goyang to Harbin radiowave propagation path**

301 The radio station operating at 6,600 kHz is located in the Republic of Korea at a range, R , of ~ 910 km from the receiver.
 302 From 05:00 UT to 08:50 UT, the Doppler measurements were not possible.

303 On 29 August 2019, the Doppler spectra represented the undisturbed state of the ionosphere. For the main ray, the
 304 Doppler shift of frequency $f_D(t) \approx 0$ Hz (Fig. 9).

305 On 30 August 2019, from 09:00 UT to 14:00 UT, the Doppler spectra showed a noticeable broadening. Over the
 306 same time period, the signal amplitude experienced an enhancement in fluctuations, attaining 15–20 dBV.

307 On 31 August 2019, from 09:00 UT to 17:00 UT, considerable, from -1.3 Hz to 0.7 Hz, variations took place in the
 308 Doppler shift of frequency, $f_D(t)$. The variations in $f_D(t)$ were observed to be quasi-periodic, with ~ 40 min periods, T , and
 309 ~ 0.2 – 0.5 Hz amplitudes, f_{Da} . From 17:30 UT to 19:00 UT, $T \approx 15$ min, and $f_{Da} \approx 0.1$ Hz; the signal amplitude exhibited
 310 sporadic changes of up to 30 dBV.

311 On 1 September 2019, over the 08:30–13:00 UT period, the $f_D(t)$ also showed significant variations, from -1.5 Hz
 312 to 0.7 Hz. The signal amplitude, $A(t)$, fluctuated wildly, up to 30 dBV.

313 On 2 and 3 September 2019, the $f_D(t)$ and $A(t)$ showed virtually no change. The state of the ionosphere along the
 314 propagation path was quiet.

315 **6.6 Ulaanbaatar to Harbin radiowave propagation path**

316 The radio station operating at 7,260 kHz is located in Mongolia at an $\sim 1,496$ km range from the receiver. It was switched off
 317 from 05:00 UT to 07:00 UT and from 18:00 UT to 20:30 UT.

318 On 29 August 2019, the Doppler spectra showed that the propagation was more likely to occur along a single ray,
 319 the $f_D(t)$ varied virtually monotonically (Fig. 10).

320 On 30 August 2019, from 12:00 UT to 15:00 UT, the $f_D(t)$ exhibited quasi-periodic variations with 20 and 40 min
 321 periods, T , and with an ~ 0.1 Hz amplitude, f_{Da} , for $T \approx 20$ min and with $f_{Da} \approx 0.3$ Hz for $T \approx 40$ min.

322 On 31 August 2019, the $f_D(t)$ fluctuated wildly and varied quasi-periodically with an ~ 20 min period, T , and an ~ 0.1
 323 Hz amplitude, f_{Da} , almost all the time; from 13:30 UT to 14:00 UT, it exhibited a sharp decrease from 0 Hz to -1.5 Hz,
 324 which was followed by a subsequent increase from -1.5 Hz to 0 Hz.

325 On 1 September 2019, during the 09:00–12:30 UT period, sharp changes in $f_D(t)$ became evident, from 0 Hz to -1.5
 326 Hz and conversely.

327 On 2 September 2019, from 11:00 UT to 15:00 UT, the $f_D(t)$ exhibited quasi-periodic variations with an ~ 20 – 25 min
 328 period, T , and an ~ 0.1 Hz amplitude, f_{Da} .

329 On 3 September 2019, from 13:00 UT to 15:00 UT, quasi-periodic variations in $f_D(t)$ with an ~ 60 min period, T , and
 330 an ~ 0.15 Hz amplitude, f_{Da} , were also observed to occur.

331 Since 30 August 2019 through 2 September 2019, an increase in the frequency and level of fluctuations in signal
 332 amplitude were noted.

333 **6.7 Yakutsk to Harbin radiowave propagation path**

334 The 7,350 kHz transmitter is located in the Russian Federation at a range, R , of $\sim 1,845$ km from the receiver. Unfortunately,
 335 the transmitter operated only over the 11:00–18:00 UT and 20:15–24:00 UT periods.

336 On 29 and 30 August 2019, the Doppler spectra and signal amplitude exhibit relatively small variations (Fig. 11).

337

338

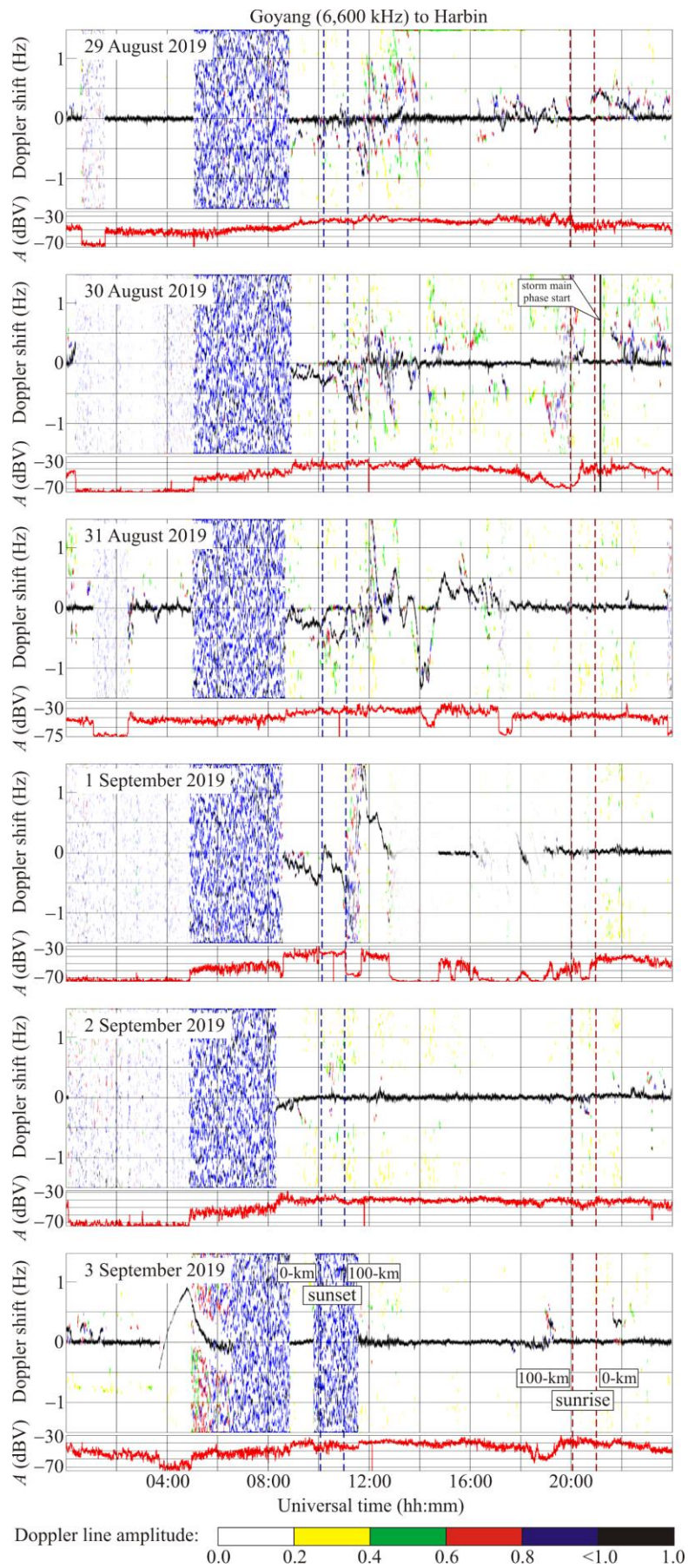


Figure 9: Same as Figure 5, but for the Goyang to Harbin radiowave propagation path at 6,600 kHz.

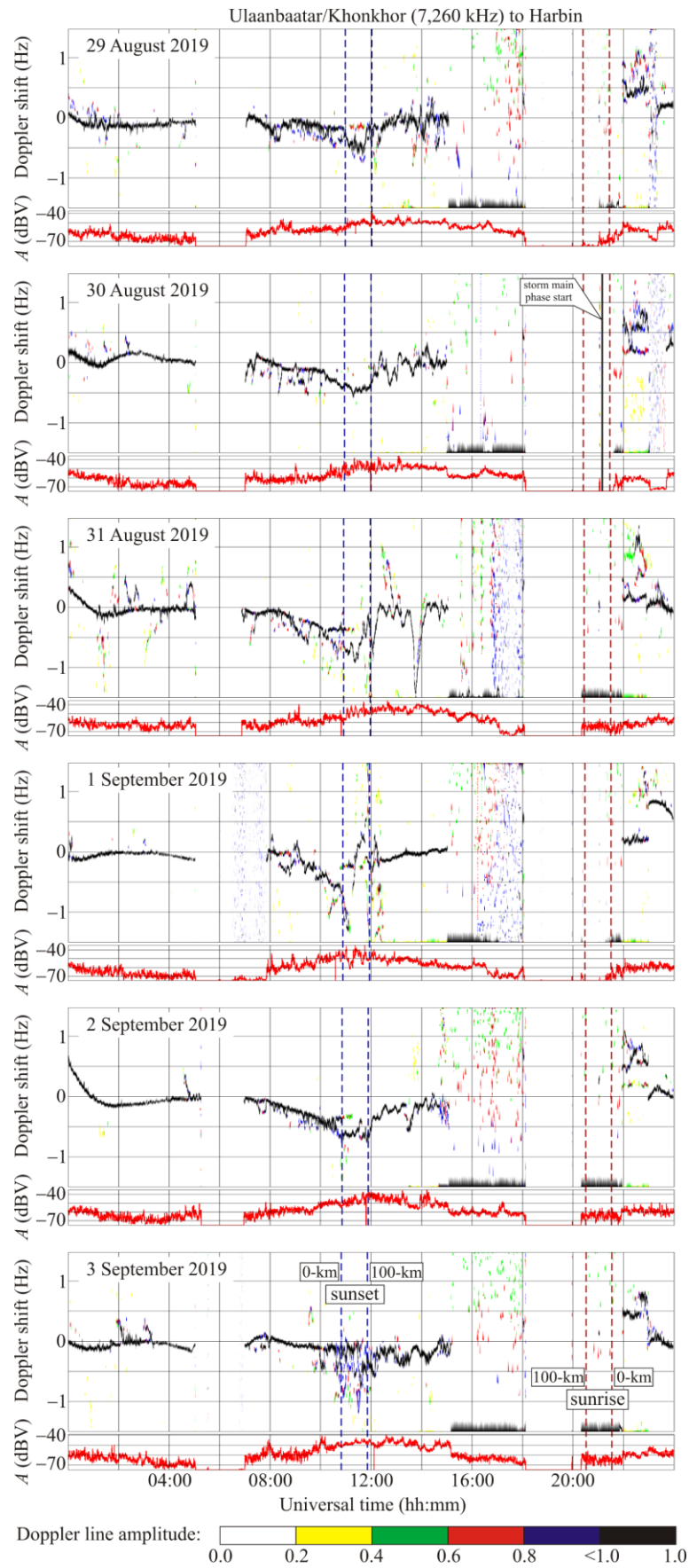


Figure 10: Same as Figure 5, but for the Ulaanbaatar/Khonkhor to Harbin radiowave propagation path at 7,260 kHz.

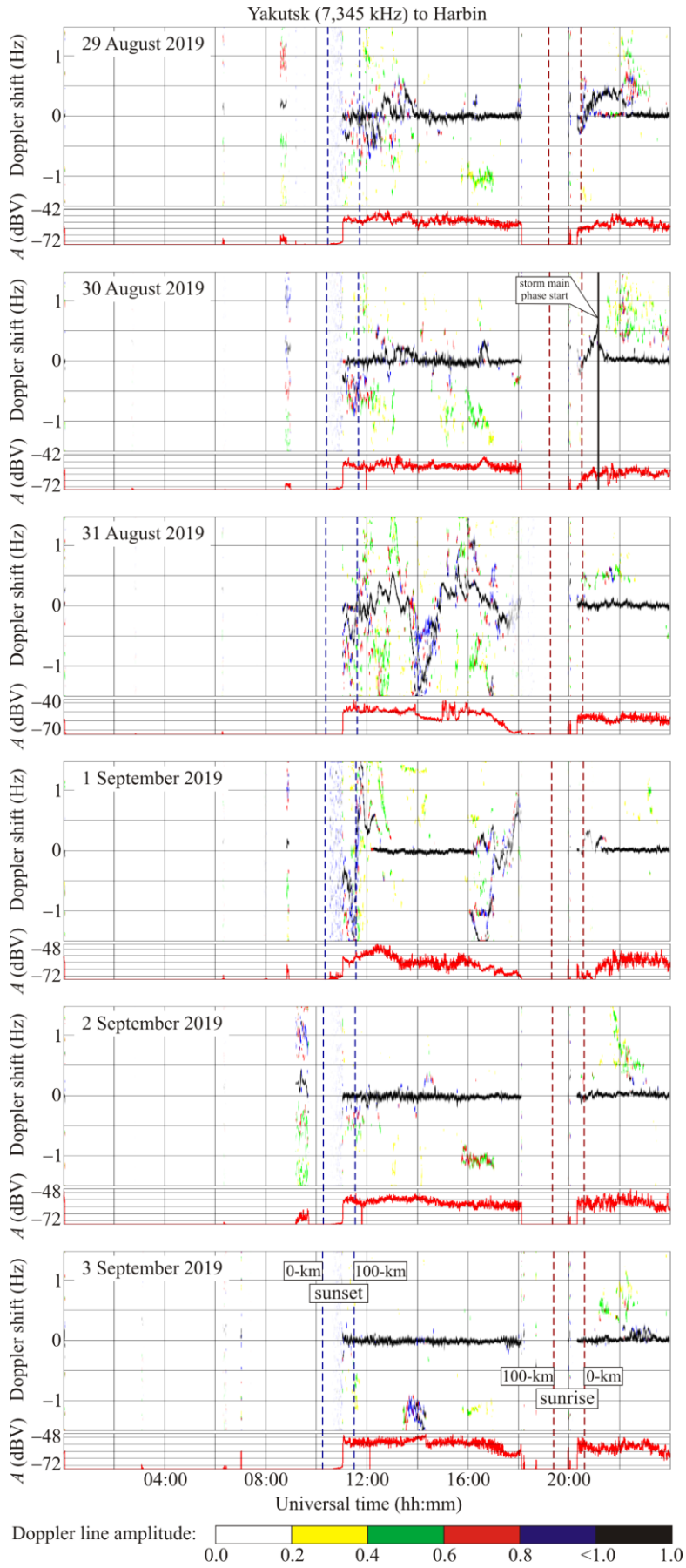


Figure 11: Same as Figure 5, but for the Yakutsk to Harbin radiowave propagation path at 7,345 kHz.

342 On 31 August 2019, the Doppler spectra occupied the -1.5 Hz to 1.5 Hz range. The $f_D(t)$ varied quasi-periodically
343 with an ~ 24 min period, T , and ~ 0.2 Hz amplitude, f_{Da} . From 13:40 UT to 14:50 UT, the $f_D(t)$ exhibited a decrease in $f_D(t)$
344 from 0 Hz to -1.5 Hz, which was followed by an increase from -1.5 Hz to 0 Hz, while the amplitude showed a decrease by
345 10 dBV. From 15:00 UT to 16:00 UT, the excursion of fluctuations in $A(t)$ attained 20 dBV.

346 On 1 September 2019, the Doppler spectra and the signal amplitudes exhibited considerable variations during the
347 11:00–13:00 UT and 16:00–18:00 UT periods. From 16:00 UT to 18:00 UT, the spectra varied quasi-periodically with 30 – 40
348 min periods, T , and 0.15 Hz amplitudes, f_{Da} .

349 On 2 and 3 September 2019, the behavior of $f_D(t)$ and $A(t)$ represented the behavior of the quiet ionosphere.

350 **6.8 Shijiazhuang to Harbin radiowave propagation path**

351 The radio station operating at $9,500$ kHz is located in the People's Republic of China at an $\sim 1,310$ km range, R , from the
352 receiver.

353 On 29 and 30 August 2019, the behaviors of the Doppler spectra and signal amplitudes were similar. The
354 ionosphere did not experience appreciable disturbances (Fig. 12).

355 On 31 August 2019, the Doppler spectra showed that the propagation is more likely to occur along a single ray. The
356 $f_D(t)$ exhibited significant variations, from -1 Hz to 0.8 Hz. Quasi-periodic variations in $f_D(t)$ with an ~ 30 min period, T , and
357 an ~ 0.3 – 0.5 Hz amplitude, f_{Da} , became evident. From 17:00 UT to 20:25 UT, $A(t) \approx -70$ dBV, the signal amplitude was
358 observed to be at the noise level. On 1 September 2019, the signal amplitude was also observed to be at the noise level
359 during the 09:10–11:50 UT and 17:00–21:40 UT periods; during the rest of the time, $f_D(t) \approx 0$ Hz.

360 The behavior of the Doppler spectra and the signal amplitudes on 2 and 3 September, 2019 was characteristic of the
361 undisturbed state of the ionosphere. Since $f_D(t) \approx 0$ Hz all the time, the radio wave was apparently reflected from the E_s layer
362 screening the ionospheric F region.

363 **6.9 Hohhot to Harbin radiowave propagation path**

364 The $9,520$ kHz transmitter is located in the People's Republic of China at an $\sim 1,340$ km range from the receiver. The radio
365 station usually does not broadcast from 16:00 UT to 21:40 UT.

366 On 29 August 2019, considerable variations in the Doppler spectra, $f_D(t)$, and the signal amplitude, $A(t)$, were
367 observed to occur near the dusk and dawn terminators in the ionosphere (Fig. 13).

368 On 30 August 2019, significant variations in the Doppler spectra became evident from 14:00 UT to 16:00 UT.

369 On 31 August 2019, considerable, from -0.7 Hz to 0.7 Hz, variations in $f_D(t)$ took place over the 11:00–13:30 UT
370 period. The period, T , is observed to be ~ 24 min, and the amplitude, f_{Da} , ~ 0.1 – 0.5 Hz.

371 On 1 September 2019, $f_D(t) \approx 0$ Hz almost all the time. Significant, 20 – 40 dBV, variations in $A(t)$ were observed to
372 occur from 08:00 UT to 16:00 UT.

373 On 2 and 3 September 2019, the ionosphere did not experience considerable disturbances.

374 **6.10 Yamata to Harbin radiowave propagation path**

375 The $9,750$ kHz transmitter is located in Japan at an $\sim 1,570$ km range, R , from the receiver. The transmissions are usually
376 absent from 16:00 UT to 22:00 UT.

377 During the local daytime on 29–31 August 2019, the Doppler shift of frequency usually fluctuated around ~ 0 Hz
378 with periods, T , of about 20 – 30 min and amplitudes, f_{Da} , of about 0.1 Hz (Fig. 14). From 10:00 UT to 14:00 UT, the Doppler
379 spectra exhibited a significant broadening, and the $f_D(t)$ showed chaotic behavior.

380 On 30 August 2019, from 12:00 UT to 16:00 UT, the signal amplitude, $A(t)$, exhibited near-quasi-periodic
381 variations with a period, T , of about 30 min and 10 – 15 dBV excursions.

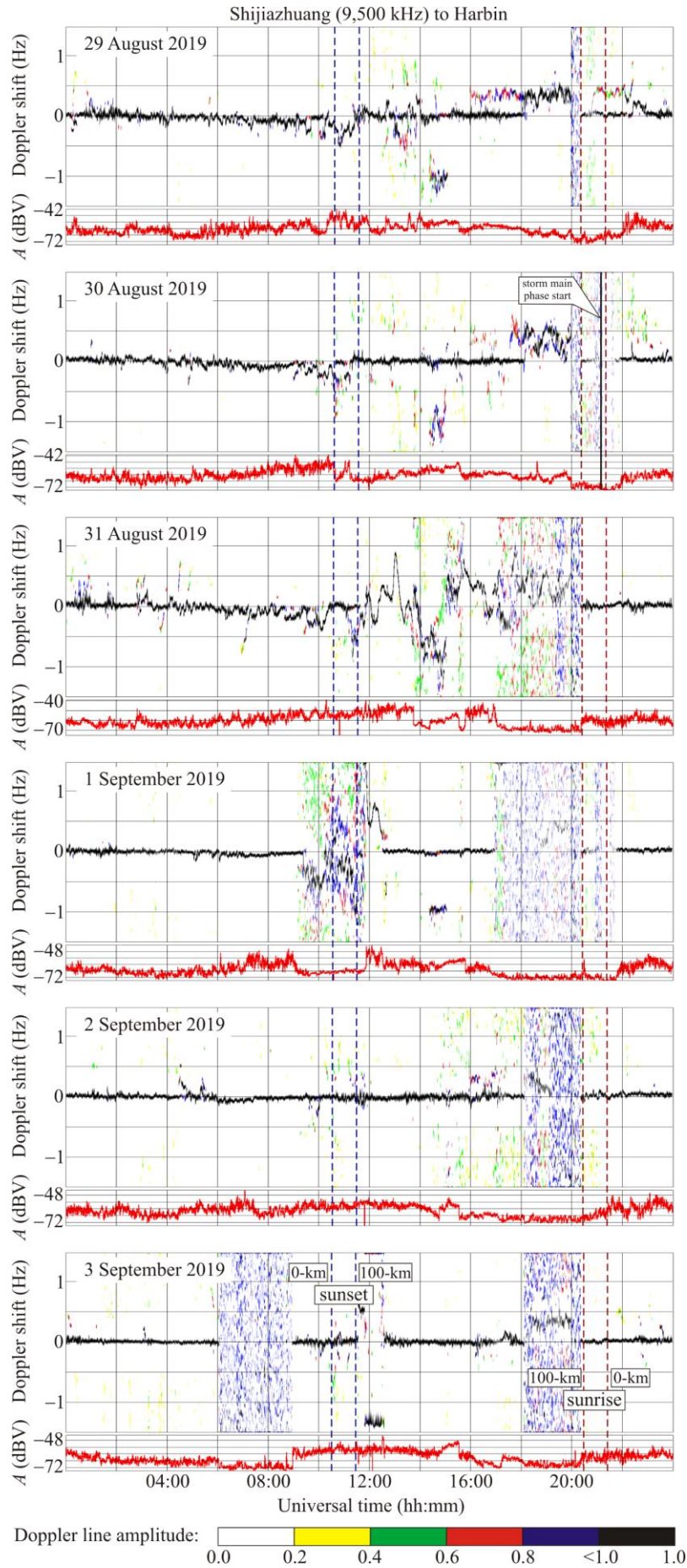


Figure 12: Same as Figure 5, but for the Shijiazhuang to Harbin radiowave propagation path at 9,500 kHz.

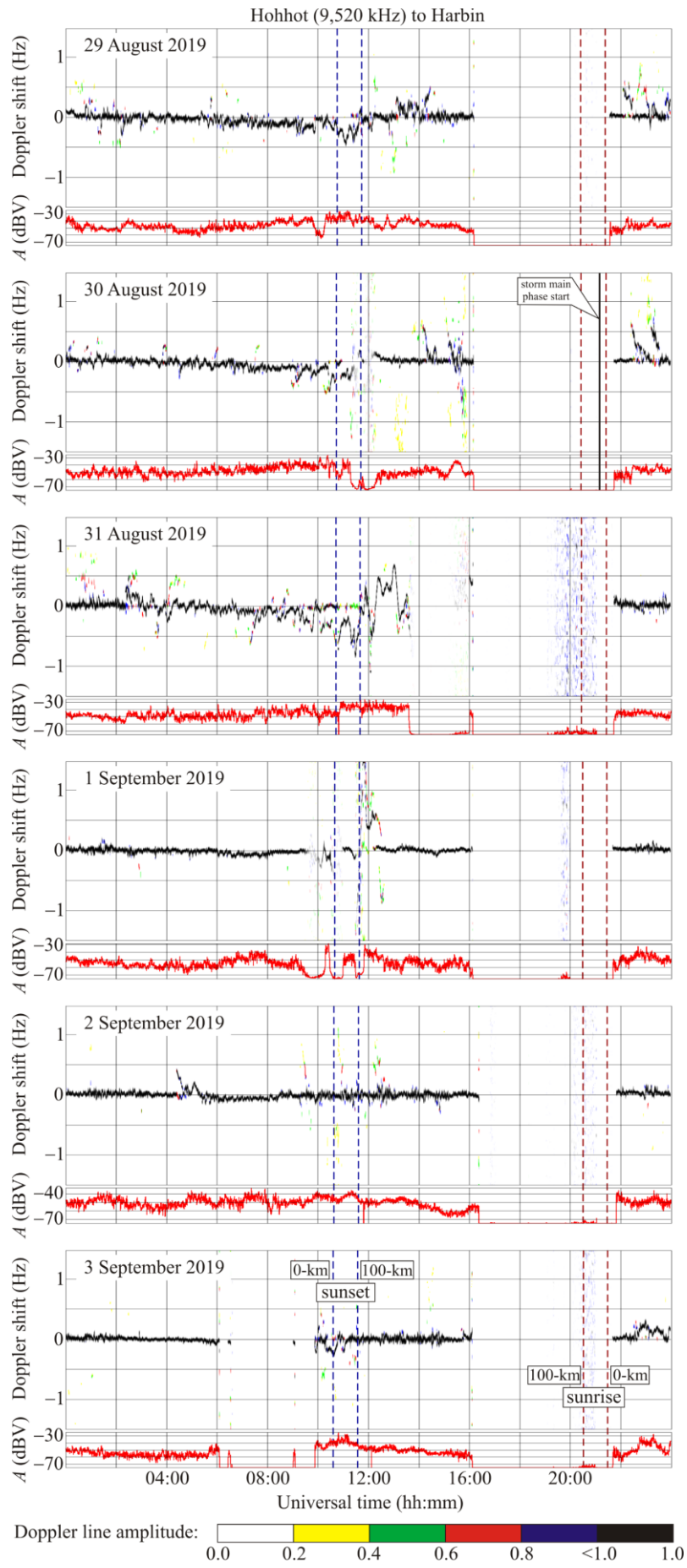


Figure 13: Same as Figure 5, but for the Hohhot to Harbin radiowave propagation path at 9,520 kHz.

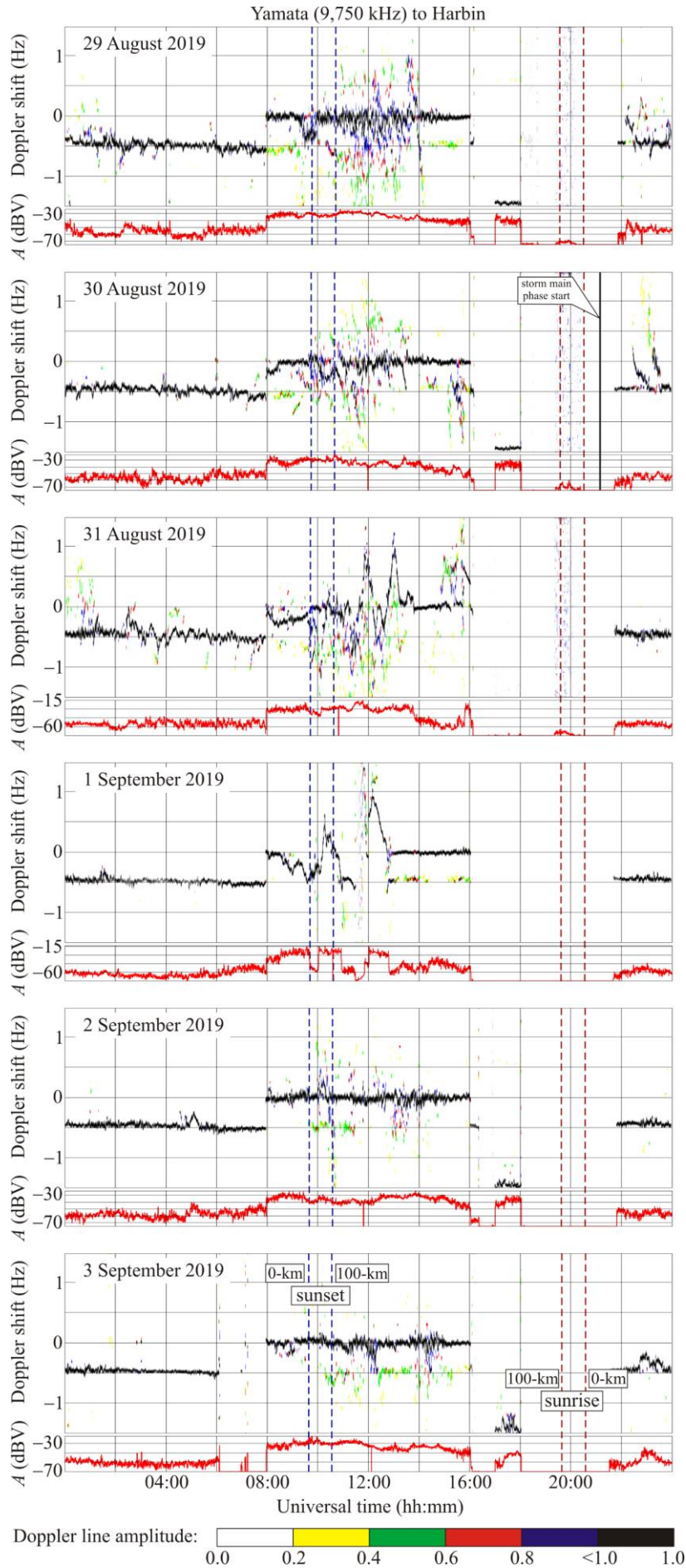


Figure 14: Same as Figure 5, but for the Yamata to Harbin radiowave propagation path at 9,750 kHz.

385 On 31 August 2019, a considerable, from -0.4 Hz to 0.8 Hz, increase of variations in $f_D(t)$ was observed to occur
386 from 12:00 UT to 16:00 UT, while the fluctuations in the signal amplitude, $A(t)$, were small, in the 10–15 dBV range.

387 On 1 September 2019, the excursions in $f_D(t)$ varied from -0.5 Hz to 1 Hz during the 08:00–13:00 UT period, while
388 the signal amplitude exhibited sharp changes, by 40–60 dBV.

389 On 2 and 3 September 2019, the $f_D(t)$ and $A(t)$ exhibited behavior characteristic of the quiet days.

390 **6.11 Beijing to Harbin radiowave propagation path**

391 The radio station broadcasting at 9,830 kHz over an interval shorter than half of a day is located in the People's Republic of
392 China at an $\sim 1,050$ km range, R , from the receiver.

393 On 29 and 30 August 2019, and on 2 and 3 September 2019, the Doppler spectra did not exhibit considerable
394 variations (Fig. 15). Their variations were observed to occur from 11:00 UT to 16:00 UT on 31 August 2019 and from 10:00
395 UT to 12:30 UT on 1 September 2019.

396 On 30 and 31 August 2019 and on 1 September 2019, the signal amplitude exhibited considerable, up to 30 dBV,
397 variations. The reflected signal was absent from 14:00 UT to 18:00 UT on 31 August 2019 and from 09:00 UT to 12:10 UT
398 on 1 September 2019.

399 **7 Discussion**

400 The strength of geospace storms is conveniently estimated by the energy entering the magnetosphere from the solar wind per
401 unit of time, the Akasofu function. The index

$$402 \quad G_{st} = 101g \frac{\varepsilon_A}{\varepsilon_{Amin}},$$

403 where $\varepsilon_{Amin} = 10 \text{ GJ s}^{-1}$, have been introduced in (Chernogor and Domnin, 2014) and is used to measure the storm strength.
404 Substituting $\varepsilon_{Amax} \approx 15 \text{ GJ s}^{-1}$ for the storm under study gives $G_{st} \approx 1.8$. According to the classification of Chernogor and
405 Domnin (2014), this storm is minor. Assuming the storm length to be $\Delta t \approx 10^5$ s, the energy entering the magnetosphere is
406 found to be $E_{st} \approx 1.5 \times 10^{15}$ J. Such a storm falls into the Geospace Storm Index 1 (GSSII) type (Chernogor and Domnin,
407 2014).

408 **7.1 Geomagnetic field effects**

409 The effects in the geomagnetic field began to appear after 12:00 UT on 30 August 2019. Considerable effects in the
410 geomagnetic field occurred during the main phase of the magnetic storm, i. e., on 31 August 2019 and 1 September 2019.
411 The recovery phase persisted for 2–3 days since 00:00 UT on 2 September 2019.

412 Let us estimate the magnetic storm energy E_{ms} and the power P_{ms} , using the relation of Gonzalez et al. (1994):

$$413 \quad E_{ms} = \frac{3}{2} E_m \frac{|D_{st}^*|}{B_0},$$

414 where $B_0 \approx 3 \times 10^{-5}$ T is the equatorial magnetic induction, and $E_m \approx 8 \times 10^{17}$ J is the total energy in the Earth's dipole
415 magnetic field.

416

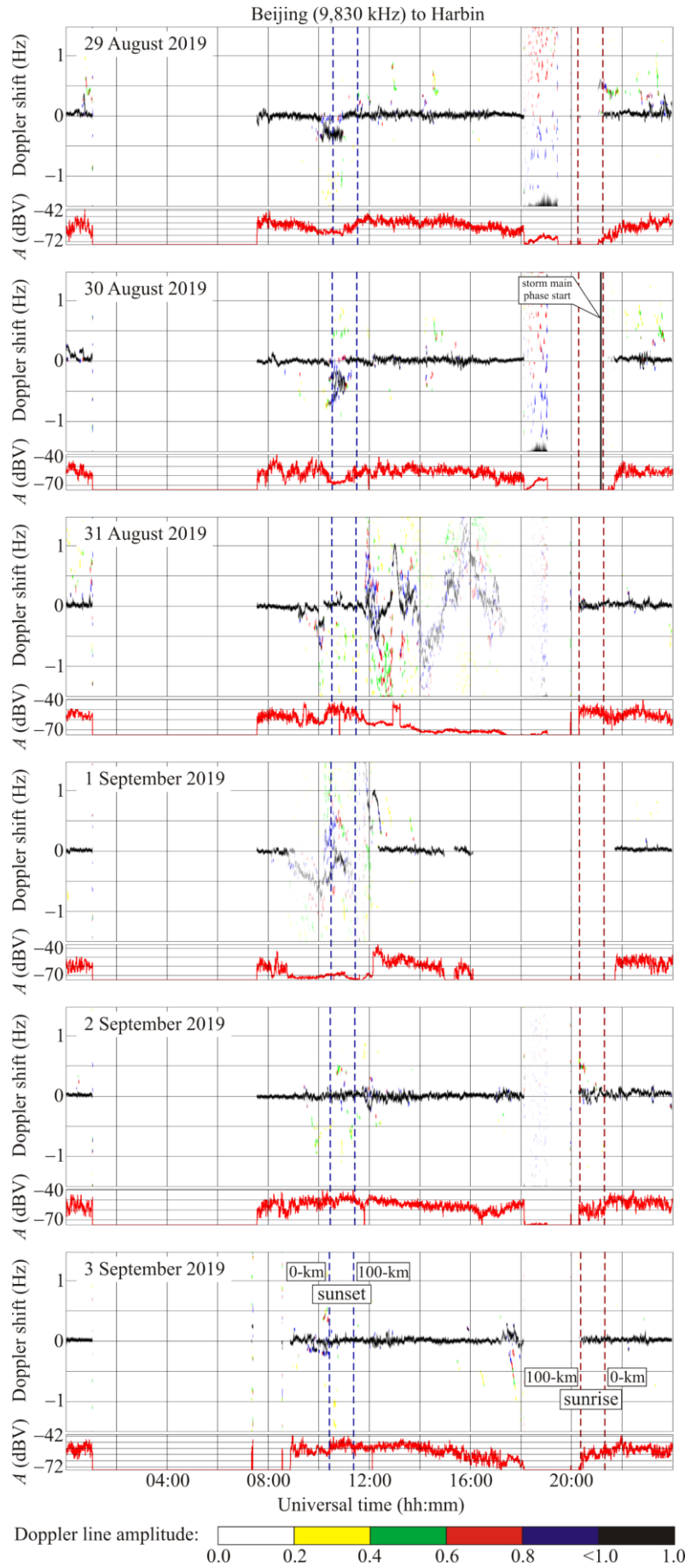


Figure 15: Same as Figure 5, but for the Beijing to Harbin radiowave propagation path at 9,830 kHz.

418 The corrected value of D_{st}^* is given by

$$419 \quad D_{st}^* = D_{st} - bp_{sw}^{1/2} + c,$$

420 where $b = 5 \times 10^5 \text{ nT (J}\cdot\text{m}^{-3})^{-1/2}$, $c = 20 \text{ nT}$, $p_{sw} = n_p m_p V_{sw}^2$, m_p and n_p are proton mass and number density, V_{sw} is the solar
421 wind bulk speed. Given $p_{sw\text{max}} \approx 3 \text{ nPa}$, $D_{st\text{min}} \approx -55 \text{ nT}$, and $D_{st}^* = -62 \text{ nT}$, the magnetic storm energy $E_{ms} = 1.5 \text{ PJ}$. For the
422 magnetic storm of $1.7 \times 10^5 \text{ s}$ duration, the power $P_{ms} \approx 9 \text{ GW}$.

423 In accordance with the NOAA Space Weather Scale [<http://www.sec.noaa.gov>], this storm is classified as moderate.
424 In accordance with the classification system of Chernogor and Domnin (2014), magnetic storms with $K_p = 5.0\text{--}5.9$ are
425 classified as moderate, and their energy and power lie within the $E_{ms} \approx (1\text{--}5) \times 10^{15} \text{ J}$ and $P_{ms} \approx (6\text{--}22) \times 10^{10} \text{ W}$ limits,
426 respectively.

427 7.2 Effects in geomagnetic field fluctuations

428 The universal time dependences of the horizontal components of the geomagnetic field in the 100–1000 s period range were
429 subjected to the systems spectral analysis in the 100–1000 s period range.

430 The results of the spectral analysis for 29 August 2019, which could be considered as reference date, are presented
431 in Fig. 16. The H - and D -component levels did not exceed 2–3 nT, while the spectra exhibited predominantly 600–900 s
432 period oscillations.

433 On 31 August 2019, the day when the storm's main phase was observed, the H - and D -components attained 5–
434 10 nT (Fig. 17). The spectra of the H - and D -components showed predominantly 300–400 s, 700–900 s and 400–600 s, 700–
435 900 s period oscillations, respectively.

436 On 1 September 2019, the levels of the components remained the same as those on 31 August 2019. The 800–1000
437 s period oscillations were predominant in both components.

438 7.3 Ionospheric storm effects

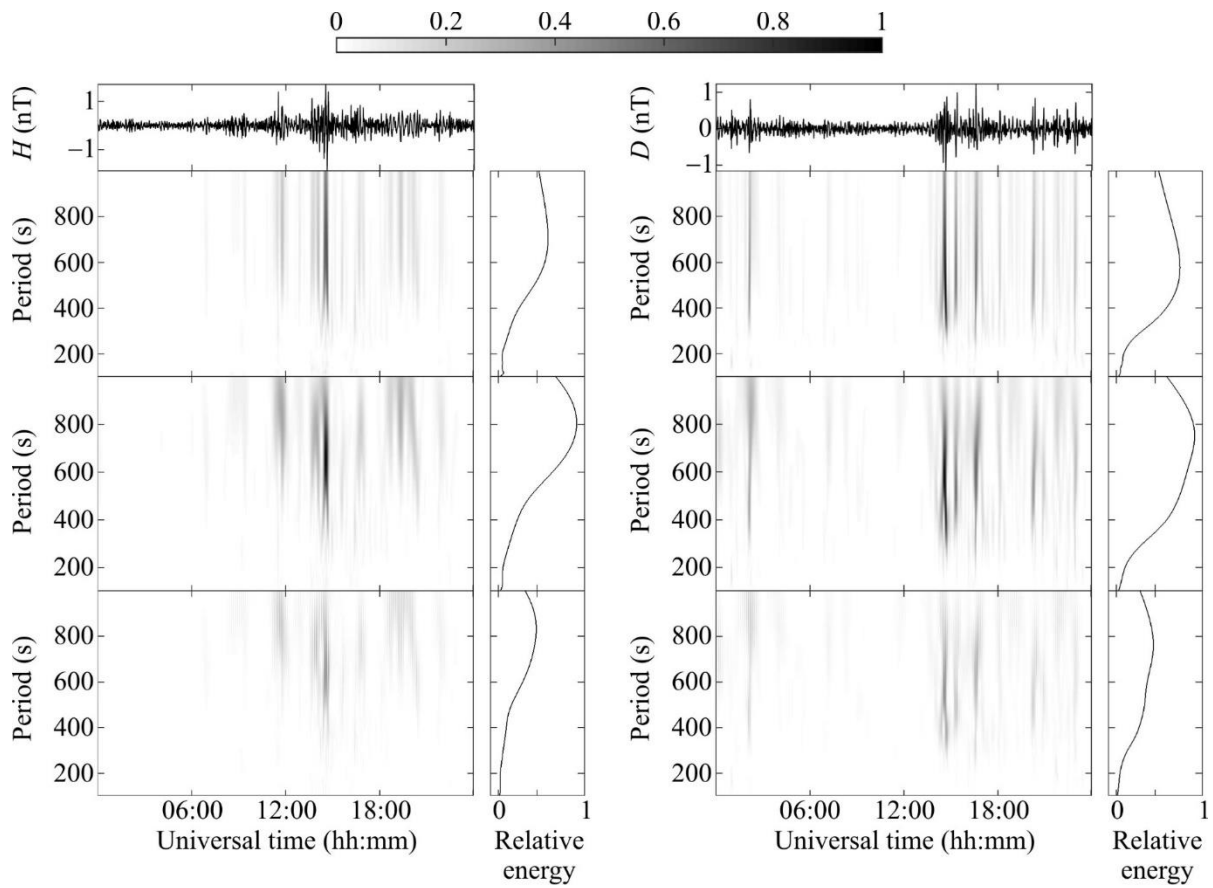
439 7.3.1 Disturbances in ionogram parameters

440 Variations in ionogram parameters observed with the Japan and Russian Federation ionosondes exhibit similar behaviors.
441 This suggests that the ionospheric storm under study is a large-scale phenomenon.

442 The list of the main effects that accompanied the ionospheric storm include the following.

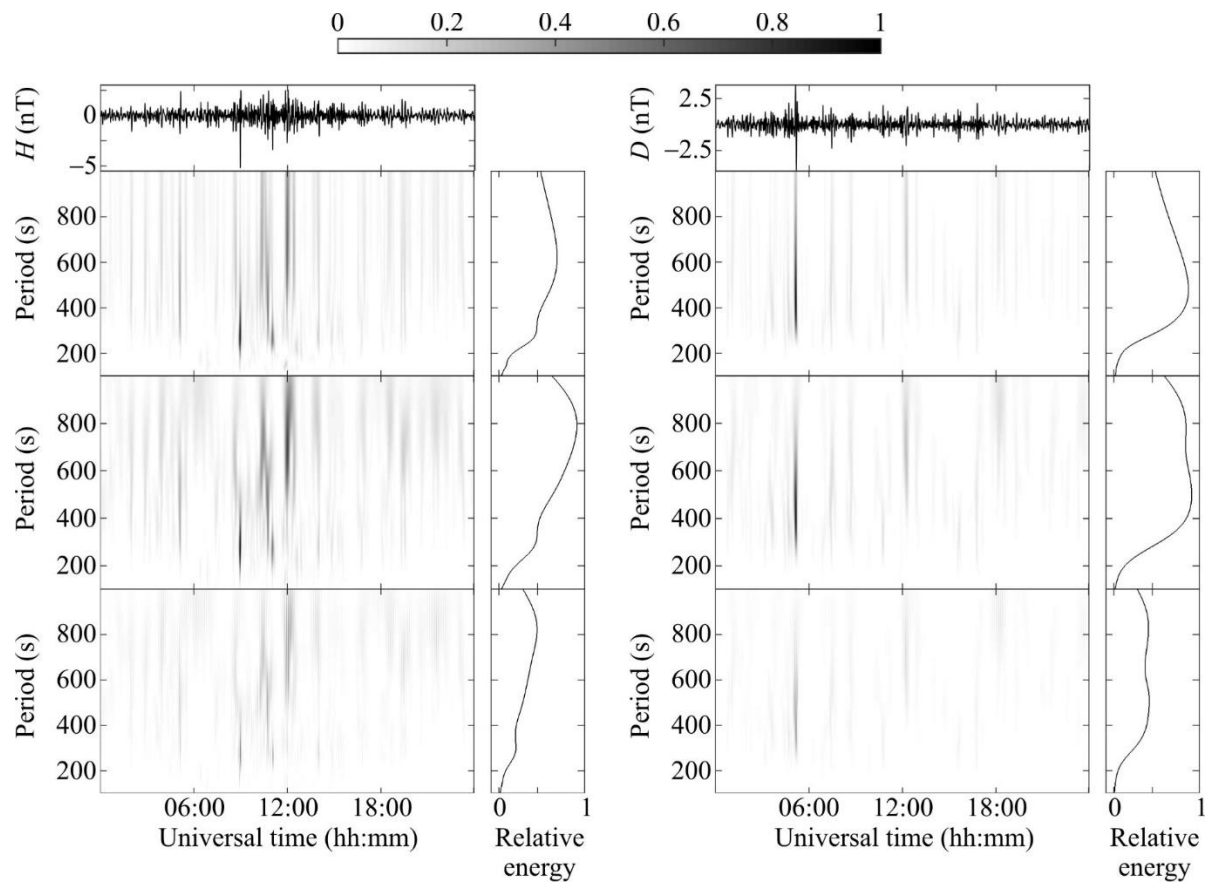
- 443 1. An increase in f_{min} from 1.4 MHz to 2.2–2.4 MHz from 07:30 UT to 08:30 UT on 31 August 2019.
- 444 2. An increase in f_{oE_s} from 3 MHz to 6–7 MHz from 05:00 UT to 08:00 UT on 31 August 2019.
- 445 3. A decrease in f_{oF_2} by 0.7–1.1 MHz 31 August 2019 as compared to f_{oF_2} on 29 August 2019.
- 446 4. A decrease in f_{oF_2} by 0.2–0.6 MHz on 1 September 2019 as compared to f_{oF_2} on 2 September 2019.
- 447 5. An increase in h'_E from 102 km to 113 km from 10:00 UT to 13:00 UT on 31 August 2019.
- 448 6. An increase in h'_E from 110 km to 133 km at approximately 12:30 UT on 1 September 2019.
- 449 7. An increase in h'_{E_s} from 105 km to 130 km from 10:00 UT to 13:00 UT on 31 August 2019.
- 450 8. An increase in h'_{E_s} from 110 km to 125–132 km from 08:00 UT to 14:00 UT on 1 September 2019.
- 451 9. Brief spikes in h'_{F_2} from 250 km to 400–450 km from 13:30 UT to 14:30 UT and from 16:00 UT to 16:30 UT on 31
452 August 2019.
- 453 10. An increase h'_{F_2} from 250–300 km to 400–500 km during the 31 August 2019/1 September 2019 night, as well as from
454 16:00 UT to 18:00 UT on 1 September 2019.

455



456

457 Figure 16: Systems spectral analysis products for the geomagnetic variations on 29 August 2019 at V. N. Karazin Kharkiv
 458 National University Magnetometer Observatory.



459

460 Figure 17: Systems spectral analysis products for the geomagnetic variations on 31 August 2019 at V. N. Karazin Kharkiv
 461 National University Magnetometer Observatory.

462

463 Analysis of the ionograms indicates that the ionospheric storm occurred mainly during the 31 August 2019 and 1
 464 September 2019 period. The storm duration virtually coincide with the duration of the magnetic storm main phase.

465 Since the f_{oF2} values on 31 August 2019 were less than those on 29 August 2019, a reference day, by 0.7–1.1 MHz,
 466 the ionospheric storm should be classified as negative. Furthermore, the f_{oF2} values on 1 September 2019, were less than
 467 those on 2 September 2019, another reference day.

468 Estimation of a decrease in the electron density, N , during the ionospheric storm as compared to the electron
 469 density, N_0 , on the reference day has been made using the following relation:

$$470 \quad \frac{N_0}{N} = \left(\frac{f_{oF20}}{f_{oF2}} \right)^2.$$

471 The dawn, daytime, and dusk N_0/N ratio for 31 August 2019 were observed to be 1.8–2, 1.4, and 2.4, respectively.

472 The dawn and daytime N_0/N ratio for 1 September 2019 was observed to be close to 1.56 and 1.16, respectively.

473 Given the N_0/N , the negative ionospheric index [Chernogor and Domnin, 2014] can be calculated

$$474 \quad I_{NIS} = 10 \lg \frac{N_0}{N_{\min}}, \text{ dB.}$$

475 For this storm, $(N_0/N_{\min}) \approx 2.4$, and $I_{NIS} \approx 3.8$ dB. In accordance with Chernogor and Domnin's classification (2014), the
 476 strength of such an ionospheric storm is classified as Negative Ionospheric Storm Index 3, NIS3. Furthermore, this geospace
 477 storm manifested itself not only in the ionospheric F region, but also in the ionospheric E region, and in sporadic E_s layer.

478 As a whole, the mechanisms for negative ionospheric storms are well known. They include an enhancement in the
 479 wind speed, traveling atmospheric disturbances propagating equatorward (Prölss, 1993a, b), composition changes in the
 480 thermosphere, and an increase from ~ 0.1 – 0.3 mV/m to 5 – 10 mV/m in an eastward zonal electric field arising during an
 481 electrical storm (see, Section 1, Introduction) that acts to decrease the electron density and to increase F_2 -layer virtual height.

482 The estimate of the ionospheric storm index and of the energy of the geospace and magnetic storms have allowed us
 483 to establish that a weak geospace storm acted to give rise to a moderate magnetic storm and to a strong ionospheric storm,
 484 which is not as trivial as may be supposed. The establishment of this fact were impossible without the quantitative estimates.

485 During ionospheric storms the phases/ionospheric response (positive and negative) are usually alternating. In most
 486 cases, the CIR storms have positive effect just after storm onset. Storms are usually accompanied by large- or medium-scale
 487 travelling ionospheric disturbances formed by GW that propagate from high latitudes toward the equator.

488 7.3.2 Radio-wave reflection height variations

489 The ionosonde data show that the virtual reflection heights h'_E , h'_{Es} , and h'_{F2} exhibit sharp brief spikes at particular times.
 490 This suggest significant changes occurring in the $N(h)$ profile. The variations in $N(h)$ acted to sharply change the Doppler
 491 shift of frequency $f_D(t)$. On 31 August 2019, at about 14:00 UT, the f_D virtually along all propagation paths exhibited a sharp
 492 decrease from 0 Hz to $-(1-1.5)$ Hz, followed by an increase from the minimum value to 0 Hz. This duration of this effect
 493 was observed to be 50 to 60 min for different propagation paths. The sharp decrease in $f_D(t)$ followed by its increase to the
 494 initial value indicates that a rise in the reflection height occurred. A rise in the altitude can be estimated by using the
 495 following simplified relation:

$$496 \quad \Delta z_r = -\frac{c}{4} \frac{\Delta f_{Dm}}{f} \left(\frac{\Delta T_1}{\cos \theta_1} + \frac{\Delta T - \Delta T_1}{\cos \theta_2} \right), \quad (1)$$

497 where c is the speed of light, Δf_{Dm} is an f_D maximum value, ΔT_1 is the duration of a decrease in $f_D(t)$, ΔT is an overall
 498 duration of the variation in f_D , $\overline{\cos \theta_1}$, and $\overline{\cos \theta_2}$ are values averaged over ΔT_1 and $\Delta T - \Delta T_1$, respectively, and θ is an angle
 499 of incidence with respect to the vertical.

500 Often, $\Delta T_1 = \Delta T - \Delta T_1$, i.e., $\Delta T_1 = \Delta T/2$. Hence, from Eq. (1), one has the relation

$$\Delta z_r = -\frac{c\Delta T}{4\cos\theta_{\text{eff}}}\frac{\Delta f_{Dm}}{f},$$

502 where

$$\frac{1}{\cos\theta_{\text{eff}}} = \frac{1}{2}\left(\frac{1}{\cos\theta_1} + \frac{1}{\cos\theta_2}\right). \quad (2)$$

504 Then it follows from Eq. (1) and Eq. (2) that the altitude of reflection increases when $\Delta f_{Dm} < 0$, and vice versa.

505 The expression in Eq. (2), when applied to the Lintong/Pucheng–Harbin propagation path where $\Delta f_{Dm} \approx -1$ Hz and
 506 $\Delta T = 60$ min for nighttime conditions, gives $\Delta z_r \approx 110$ km, i.e., the altitude exhibits an increase from ~ 150 km to ~ 260 km.
 507 For the Hwaseong–Harbin propagation path, when $\Delta f_{Dm} \approx -1$ Hz and $\Delta T \approx 60$ min, the level of reflection shifts upward in
 508 altitude from 150 km to 300–310 km. Regarding the mechanism for an increase in the height of reflection from 150 km to
 509 300 km, such a large increase was observed at one time, 14:00 UT on August 31, 2019, when a few causes merged together.
 510 First, the rearrangement of the evening ionosphere into the night ionosphere had been completed, which was accompanied
 511 by a decrease in the electron density and an increase in the height of reflection. Second, due to the processes referred to
 512 above, the negative ionospheric storm ensued. Third, a large negative half-wave of the quasi-periodic disturbance had
 513 arrived, which was observed along all radio wave propagation paths from about 12:00 UT to 16:00 UT. Variations in the
 514 height of reflection that occurred over other time intervals were observed to occur within the 30–50 km limits.
 515 The altitudes of reflection along other propagation paths were estimated to be of the same order of magnitude. This effect is
 516 also a manifestation of the ionospheric storm.

517 7.3.3 Wavelike disturbance effects

518 The ionospheric storm was accompanied by the generation of quasi-periodic variations in the Doppler shift of frequency.
 519 From 12:00 UT to 17:00 UT on 31 August 2019, virtually all propagation paths exhibited a quasiperiodicity in $f_D(t)$ at ~ 30
 520 min period, T , and ~ 0.4 – 0.6 Hz amplitude, f_{Da} . Given the f_{Da} , the amplitude of variations in the electron density can be
 521 estimated by employing the following relation (Guo et al., 2019a, 2020; Chernogor et al., 2020):

$$\delta_{Na} = \frac{K}{4\pi} \frac{cT}{L} \frac{f_{Da}}{f}, \quad (3)$$

523 where $K = \frac{1 + \sin\theta}{(1 + 2\zeta \tan^2\theta)\cos\theta}$, $\zeta = \frac{z_r}{r_0}$, $\tan\theta = \frac{R}{2z_r}$, $L = \frac{2HL_n}{2H + L_n}$, z_r is the altitude of reflection, r_0 is the Earth's radius, H

524 is the scale height of the atmosphere, L_n is a characteristic scale length of changes in the refractive index in the ionosphere.

525 The expression in Eq. (3) suggests that

$$\delta_N(t, z) = \delta_{Na}(z_0) e^{(z-z_0)/2H} \cos \frac{2\pi t}{T},$$

527 where z_0 is a reference height, e.g., 100 km.

528 Applying the expression in Eq. (3) to, for example, the Hwaseong–Harbin propagation path, where $z_r \approx 150$ km, $f_{Da} = 0.4$ Hz,
 529 $T = 30$ min, and $L \approx 30$ km, yields $\delta_{Na} \approx 42\%$. Along the Goyang–Harbin propagation path over the 17:30–20:00 UT period,
 530 an oscillation with ~ 15 min period, T , and 0.1 Hz amplitude, f_{Da} , was observed to occur. Substituting $z_r \approx 200$ km and $L \approx 80$
 531 km in Ed. (3) leads to $\delta_{Na} \approx 6\%$.

532 The magnitudes of periods, of ~ 15 – 60 min, and of the amplitudes δ_{Na} suggest that the quasi-periodic variations in
 533 $f_D(t)$ and $N(t)$ launched atmospheric gravity waves (AGWs). It is well known that AGWs are generated in the auroral oval in
 534 the course of geospace storms and propagate to low latitudes (see, for example, Hajkowicz, 1991; Lei et al., 2008; Lyons et
 535 al., 2019). We have tried to find a confirmation of this fact in our measurements. For example, the minimum magnitude of
 536 the Doppler shift of frequency along the Ulaanbaatar to Harbin (7,260 kHz) propagation path is observed to occur at

537 approximately 12:47 UT, and along the Beijing to Harbin (6,175 kHz) propagation path at 13:00 UT. Taking into account the
538 distance of 400 km between the propagation path midpoints in the equatorward direction yields the equatorward speed of
539 510 m/s. Such speeds and periods of tens of minutes are inherent in atmospheric gravity waves. Thus, the generation of
540 AGWs responsible for traveling ionospheric disturbances is also a manifestation of geospace storms.

541 The studies presented at this paper demonstrate conclusively that the multi-frequency multipath facility involving
542 the software-defined technology for sounding obliquely the ionosphere at the Harbin Engineering University is an effective
543 means for investigating the influence of ionospheric storms on the characteristics of HF radio waves and the short-term
544 variability of dynamic processes operating in the ionosphere.

545 **8 Conclusions**

546 1. The energy and power of the geospace storm have been estimated to be 1.5×10^{15} J and 1.5×10^{10} W, which means that
547 this storm is classified as weak.

548 2. The energy and power of the magnetic storm have been estimated to be 1.5×10^{15} J and 9×10^9 W, which means that this
549 storm is classified as moderate. The storm's main feature is its main phase duration, of up to two days. The recovery phase
550 was also long, no less than two days.

551 3. In the course of 31 August 2019 and 1 September 2019, the *H*- and *D*-component disturbances attained 60–70 nT. The *Z*-
552 component variations did not exceed 20 nT.

553 4. On 31 August 2019 and 1 September 2019, the level of fluctuations in the geomagnetic field in the 1–1000 s period range
554 exhibited an increase from 0.2–0.3 nT to 2–4 nT. The oscillations in the 300–400 s to 700–900 s period range had maximum
555 energy.

556 5. The geospace storm was accompanied by a moderate to strong negative ionospheric storm. In the course of the 31
557 August–1 September 2019 period, the electron density in the ionospheric *F* region exhibited a decrease by a factor of 1.4 to
558 2.4 times as compared to that on the reference day.

559 6. The geospace storm acted to notably disturb the ionospheric *E* region, as well as sporadic *E_s* layer.

560 7. In the course of the ionospheric storm, the altitude of reflection of radio waves could exhibit sharp increases from ~150
561 km to ~300–310 km.

562 8. The geospace storm was accompanied by the generation of AGWs, which modulate the electron density in the ionosphere.
563 The amplitude of the disturbances in the electron density could attain ~42 %, at ~30 min period, while at ~15 min period, it
564 did not exceed 6 %.

565

566 **Code availability**

567 The doppler14.grc file contains the computer program code that generates the data from the raw data recorded by the multi-
568 frequency multipath system at the Harbin Engineering University campus, the People's Republic of China (45.78° N,
569 126.68° E). These data are needed to plot the Doppler shift of frequency and the amplitude presented in Figures 5–15 (see
570 the SupplementaryMaterial.zip file).

571

572 **Data availability**

573 The raw data sets recorded by the multi-frequency multipath system at the Harbin Engineering University campus, the
574 People's Republic of China (45.78° N, 126.68° E) and discussed in this paper can be requested online at
575 <https://dataverse.harvard.edu/dataset.xhtml?persistentId=doi:10.7910/DVN/86LHDC> (Luo et al., 2020b).

576 Citation:

577 Luo, Y., Chernogor, L., Garmash, K., Guo, Q., Rozumenko, V., Zheng, Y.: RAW Data on Parameters of Ionospheric HF
578 Radio Waves Propagated Over China During the August 30–September 2, 2019 Geospace Storm,
579 <https://dataverse.harvard.edu/dataset.xhtml?persistentId=doi:10.7910/DVN/86LHDC>, 2020b.
580

581 **Author contribution.** <https://casrai.org/credit/>
582 Yiyang Luo processed the data observed. Leonid Chernogor interpreted the physics of the observations, wrote Sections 1, 6,
583 7, and 8. Kostiantyn Garmash developed the software, processed the data, wrote Sub-sections 2.1. Qiang Guo developed the
584 software, conducted uninterrupted observations. Victor Rozumenko wrote Section 3, and Subsections 4.1, 4.2, 5.2. Yu Zheng
585 wrote Subsections 2.2, 5.1. All co-authors took part in the discussion of the results obtained.
586

587 **Competing interests**
588 The authors declare that they have no conflict of interest.
589

590 **Acknowledgments.** The solar wind parameters have been retrieved from the Goddard Space Flight Center Space Physics
591 Data Facility <https://omniweb.gsfc.nasa.gov/form/dx1.html>. This publication makes use of the data recorded at the Low
592 Frequency Observatory, owned by the Institute of Radio Astronomy NASU, Radiophysics of Geospace Department,
593 Laboratory of Electromagnetic Surrounding of the Earth. The authors thank the staff of the Observatory for its operation
594 (magnetometer data are retrieved from <http://geospace.com.ua/en/observatory/metmag.html>). This research also draws upon
595 data provided by the WK546 URSI code ionosonde at the City of Wakkanai (45.16° N, 141.75° E), Japan, URL:
596 wdc.nict.go.jp/IONO/HP2009/contents/Ionosonde_Map_E.html. Ionosonde data from the City of Moscow, the Russian
597 Federation (55.47° N, 37.3° E), are retrieved from
598 <https://lgdc.uml.edu/common/DIDBYearListForStation?ursiCode=MO155>. Graduate student Luo Yiyang thanks the China
599 Scholarship Council (CSC) program (201908100008) for the financial support. Work by Qiang Guo and Yu Zheng was
600 supported by National key R & D plan strategic international science and technology cooperation and innovation
601 (2018YFE0206500). Work by L. F. Chernogor and Y. Luo was supported by the National Research Foundation of Ukraine
602 for financial support (project 2020.02/0015, "Theoretical and experimental studies of global disturbances from natural and
603 technogenic sources in the Earth-atmosphere-ionosphere system"). Work by L. F. Chernogor, K. P. Garmash, and by V. T.
604 Rozumenko was supported by Ukraine state research project #0119U002538.

605 **References**

606 Appleton, E. and Ingram, L.: Magnetic storms and upper atmospheric ionization, *Nature*, 136, 548–549,
607 <https://doi.org/10.1038/136548b0>, 1935.
608 Benestad, R. E.: Solar activity and Earth's climate, Springer-Praxis, 316 p. <http://doi.org/10.1007/3-540-30621-8>, 2006.
609 Blagoveshchensky, D. and Sergeeva, M.: Impact of geomagnetic storm of September 7–8, 2017 on ionosphere and HF
610 propagation: A multi-instrument study, *Advances in Space Research*, 63 (1), 239–256,
611 <https://doi.org/10.1016/j.asr.2018.07.016>, 2019.
612 Blanch, E., Altadill, D., Boška, J., Burešová, D., and Hernández-Pajares, M.: November 2003 event: Effects on the Earth's
613 ionosphere observed from ground-based ionosonde and GPS data. In: *Annales Geophysicae*, 23, 3027–3034. 2005.
614 Borries, C., Berdermann, J., Jakowski, N., and Wilken, V.: Ionospheric storms – A challenge for empirical forecast of the
615 total electron content, *Journal of Geophysical Research: Space Physics*, 120 (4), 3175–3186.
616 <https://doi.org/10.1002/2015JA020988>, 2015.
617 Bothmer, V. and Daglis, I.: *Space Weather: Physics and Effects*, Springer-Verlag Berlin Heidelberg, ISBN 3-642-06289-X.
618 2007.
619 Buonsanto, M.: Ionospheric storms – A review, *Space Science Reviews*, 88, 3–4, 563–601,
620 <https://doi.org/10.1023/A:1005107532631>, 1999.
621 Carlowicz, M. J. and Lopez, R. E.: *Storms from the Sun*, 1st edition, Joseph Henry Press, Washington DC, 256 p.
622 ISBN 0-309-07642-0. 2002.

623 Chernogor, L. F.: Advanced Methods of Spectral Analysis of Quasiperiodic Wave-Like Processes in the Ionosphere:
624 Specific Features and Experimental Results, *Geomag. Aeron.*, 48 (5), 652–673,
625 <https://doi.org/10.1134/S0016793208050101>, 2008.

626 Chernogor, L. F. and Rozumenko, V. T.: Earth–Atmosphere–Geospace as an Open Nonlinear Dynamical System, *Radio*
627 *Phys. Radio Astron.*, 13 (2), 120–137, 2008.

628 Chernogor, L. F.: The Earth-atmosphere-geospace system: main properties and processes, *International Journal of Remote*
629 *Sensing*, 32 (11), 3199–3218, <https://doi.org/10.1080/01431161.2010.541510>, 2011.

630 Chernogor, L. F.: Geomagnetic field effects of the Chelyabinsk meteoroid, *Geomagnetism and Aeronomy*, 54 (5), 613–624.
631 <https://doi.org/10.1134/S001679321405003X>, 2014.

632 Chernogor L. F., Garmash K. P., Guo Q., Luo Y., Rozumenko V. T., Zheng Y. Ionospheric storm effects over the People's
633 Republic of China on 14 May 2019: Results from multipath multi-frequency oblique radio sounding // *Advances in Space*
634 *Research*. 66 (2), 226 – 242. DOI: [10.1016/j.asr.2020.03.037](https://doi.org/10.1016/j.asr.2020.03.037), 2020.

635 Chernogor, L. and Rozumenko, V.: Physical effects in the geospace environment under quiet and disturbed conditions,
636 *Space Research in Ukraine. The Edition Report Prepared by the Space Research Institute of NAS of Ukraine and NSA of*
637 *Ukraine*, 22–34, 2011.

638 Chernogor, L. and Rozumenko, V.: Features of Physical Effects in the Geospace Environment under Quiet and Disturbed
639 Conditions, *Space Research in Ukraine 2010–2012. The Report Prepared by Space Research Institute. Kyiv*, 29–46, 2012.

640 Chernogor, L. F. and Domnin, I. F.: Physics of geospace storms, V. N. Karazin Kharkiv National University, Kharkiv, 408
641 p., 2014 (in Russian).

642 Chernogor, L. and Rozumenko, V.: Study of Physical Effects in the Geospace Environment under Quiet and Disturbed
643 Conditions, *Space Research in Ukraine 2012–2014. The Report Prepared by Space Research Institute, Kyiv*, 13–20, 2014.

644 Chernogor, L. and Rozumenko, V.: Results of the investigation of physical effects in the geospace environment under quiet
645 and disturbed conditions, National Academy of Science of Ukraine. State Space Agency of Ukraine, Kyiv,
646 *Akademperiodyka*, 23–30, 2016.

647 Chernogor, L. and Rozumenko, V.: Results of the Investigation of Physical Effects in the Geospace Environment under
648 Quiet and Disturbed Conditions, *Space Research in Ukraine 2016–2018, Report to COSPAR, Kyiv*, 41–51, 2018.

649 Chernogor, L. F., Garmash, K. P., Guo, Q., Rozumenko, V. T., and Zheng, Y.: Physical Effects of the Severe Ionospheric
650 Storm of 26 August 2018, Fifth UK–Ukraine–Spain Meeting on Solar Physics and Space Science. Programme, Abstracts,
651 information, 33, 2019a.

652 Chernogor, L. F., Garmash, K. P., Guo, Q., Rozumenko, V. T., and Zheng, Y.: Physical Processes Operating in the
653 Ionosphere after the Earthquake of Richter Magnitude 5.9 in Japan on July 7, 2018, *Astronomy and Space Physics in the*
654 *Kyiv University. Book of Abstracts. International Conference. May 28–May 31, 2019*, 87–88, 2019b.

655 Chernogor, L. F., Garmash, K. P., Guo, Q., Rozumenko, V. T., and Zheng, Y.: Effects of the Severe Ionospheric Storm of 26
656 August 2018, *Astronomy and Space Physics in the Kyiv University. Book of Abstracts. International Conference. May 28–*
657 *May 31, 2019*, 88–90, 2019c.

658 Chernogor, L. F., Garmash, K. P., Guo, Q., Luo Y., Rozumenko, V. T., and Zheng, Y.: Ionospheric storm effects over the
659 People's Republic of China on 14 May 2019: Results from multipath multi-frequency oblique radio sounding, *Adv. Space*
660 *Res.*, 66 (2), 226–242, DOI: [10.1016/j.asr.2020.03.037](https://doi.org/10.1016/j.asr.2020.03.037), 2020.

661 Danilov, A. D. Reaction of F region to geomagnetic disturbances (in Russian), *Heliogeophysical Research*, No. 5, pp. 1–33,
662 2013. <https://www.elibrary.ru/item.asp?id=21273665>

663 Danilov, A. D. and Lastovička, J.: Effects of geomagnetic storms on the ionosphere and atmosphere, *Int. J. Geomag. Aeron.*,
664 2 (3), 209–224, 2001.

665 Danilov, A. D. and Morozova, L. D.: Ionospheric storms in the F_2 region. Morphology and physics (review) (in Russian),
666 Geomagnetism and Aeronomy, 25 (5), 705–721, 1985.

667 Feldstein, Y.I., Dremukhina, L.A., Levitin, A.E., Mall, U., Alexeev, I.I., and Kalegaev, V.V.: Energetics of the
668 magnetosphere during the magnetic storm, J. Atmos. Terr. Phys., 65 (4), 429–446, ISSN 1364-6826,
669 [https://doi.org/10.1016/S1364-6826\(02\)00339-5](https://doi.org/10.1016/S1364-6826(02)00339-5), 2003.

670 Freeman, J. W.: Storms in Space, 1st edition, Cambridge University Press, London, New York, 162 p., 2001.

671 Fuller-Rowell, T. J., Codrescu, M. V., Roble, R. G., and Richmond, A. D.: How does the thermosphere and ionosphere react
672 to a geomagnetic storm? Magnetic Storms. American Geophysical Union, Washington, 203–226,
673 <https://doi.org/10.1029/GM098p0203>, 1997.

674 Gonzalez, W. D., Jozelyn, J. A., Kamide, Y., Kroehl, H. W., 1994. What is a geomagnetic storm? J. Geophys. Res. 99 (A4),
675 5771–5792. <https://doi.org/10.1029/93JA02867>

676 Goodman, J. M.: Space Weather and Telecommunications, Springer-Verlag US, XX, 382 p. <http://doi.org/10.1007/b102193>,
677 2005.

678 Guo, Q., Chernogor, L. F., Garmash, K. P., Rozumenko, V. T., and Zheng, Y.: Dynamical processes in the ionosphere
679 following the moderate earthquake in Japan on 7 July 2018, Journal of Atmospheric and Solar-Terrestrial Physics, 186, 88–
680 103, <https://doi.org/10.1016/j.jastp.2019.02.003>, 2019a.

681 Guo Q., Chernogor, L. F., Garmash, K. P., Rozumenko, V. T., and Zheng, Y.: Radio Monitoring of Dynamic Processes in
682 the Ionosphere over China during the Partial Solar Eclipse of 11 August 2018, Radio Science, 55 (2), e2019RS006866.
683 <https://doi.org/10.1029/2019RS006866>, 2020.

684 Guo, Q., Zheng, Y., Chernogor, L. F., Garmash, K. P., and Rozumenko, V. T.: Passive HF Doppler Radar for Oblique-
685 Incidence Ionospheric Sounding, 2019 IEEE 2nd Ukraine Conference on Electrical and Computer Engineering. Lviv,
686 Ukraine, July 2–6, 2019, 88–93, <https://doi.org/10.1109/UKRCON.2019.8879807>, 2019b.

687 Guo, Qiang, Zheng, Yu, Chernogor, L. F., Garmash, K. P., and Rozumenko, V. T.: Ionospheric processes observed with the
688 passive oblique-incidence HF Doppler radar, Visnyk of V. N. Karazin Kharkiv National University, series “Radio Physics
689 and Electronics”, 30, 3–15, <https://doi.org/10.26565/2311-0872-2019-30-01>, 2019c.

690 Hafstad, L. and Tuve, M.: Further studies of the Kennelly-Heaviside layer by the echo-method, Proceedings of the Institute
691 of Radio Engineers, 17 (9), 1513–1521, <https://doi.org/10.1109/JRPROC.1929.221853>, 1929.

692 Hajkowicz, L.: Auroral electrojet effect on the global occurrence pattern of large scale travelling ionospheric disturbances,
693 Planetary and Space Science, 39 (8), 1189–1196, [https://doi.org/10.1016/0032-0633\(91\)90170-F](https://doi.org/10.1016/0032-0633(91)90170-F), 1991.

694 Kamide, Y. and Maltsev, Y. P.: Geomagnetic Storms. In: Y. Kamide / A. Chian. Handbook of the Solar–Terrestrial
695 Environment, Springer–Verlag Berlin Heidelberg, 355–374, https://doi.org/10.1007/11367758_14, 2007.

696 Knipp, D.J. and Emery, B.A.: A report on the community study of the early November 1993 geomagnetic storm, Advances
697 in Space Research, 22 (1), 41–54, DOI: 10.1016/S0273-1177(97)01098-3, 1998.

698 Koskinen, H.E.J.: Physics of space storms. From Solar Surface to the Earth, Springer in association with Praxis Publishing,
699 DOI:10.1007/978-3-642-00319-6, 2011.

700 Laštovička, J.: Effects of geomagnetic storms in the lower ionosphere, middle atmosphere and troposphere, J. Atmos. Terr.
701 Phys., 58 (7), 831–843, [https://doi.org/10.1016/0021-9169\(95\)00106-9](https://doi.org/10.1016/0021-9169(95)00106-9), 1996.

702 Lathuillière, C., Menvielle, M., Lilensten, J., Amari, T., and Radicella, S. M.: From the Sun’s atmosphere to the Earth’s
703 atmosphere: an overview of scientific models available for space weather developments, Annales Geophysicae, 20 (7),
704 1081–1104, <https://doi.org/10.5194/angeo-20-1081-2002>, 2002.

705 Lei, J., Burns, A. G., Tsugawa, T., Wang, W., Solomon, S. C., and Wiltberger, M.: Observations and simulations of
706 quasiperiodic ionospheric oscillations and large-scale traveling ionospheric disturbances during the December 2006
707 geomagnetic storm, J. Geophys. Res., 113 (A6), A06310, <http://doi.org/10.1029/2008JA013090>, 2008.

708 Lilensten, J. and Bornarel, J.: *Space Weather. – Environment and Societies*, Springer, Dordrecht, Netherlands, X, 242 p.
709 <https://doi.org/10.1007/1-4020-4332-5>, 2006. ISBN 978-1-4020-4331-4.

710 Liu, J., Wang, W., Burns, A., Yue, X., Zhang, S., Zhang, Y., and Huang, C.: Profiles of ionospheric storm-enhanced density
711 during the 17 March 2015 great storm, *J. Geophys. Res.*, 121 (1), 727–744. <http://doi.org/10.1002/2015JA021832>, 2016.

712 Luo, Y., Chernogor, L. F., Garmash, K. P., Guo, Q., Rozumenko, V. T., Shulga, S. N., Zheng, Y.: Ionospheric effects of the
713 Kamchatka meteoroid: Results from multipath oblique sounding, *J. Atmos. Solar-Terr. Phys.*, 207 (10) 105336.
714 <https://doi.org/10.1016/j.jastp.2020.105336>, 2020a.

715 Luo, Y., Chernogor, L., Garmash, K., Guo, Q., Rozumenko, V., Zheng, Y.: RAW Data on Parameters of Ionospheric HF
716 Radio Waves Propagated Over China During the 30 August–September 2, 2019 Geospace Storm,
717 <https://dataverse.harvard.edu/dataset.xhtml?persistentId=doi:10.7910/DVN/86LHDC>, 2020b.

718 Lyons, L. R., Nishimura, Y., Zhang, S.-R., Coster, A. J., Bhatt, A., Kendall, E., and Deng, Y.: Identification of auroral zone
719 activity driving largescale traveling ionospheric disturbances, *Journal of Geophysical Research: Space Physics*, 124 (1),
720 700–714, <https://doi.org/10.1029/2018JA025980>, 2019.

721 Matsushita, S.: A study of the morphology of ionospheric storms, *Journal of Geophysical Research*, 64 (3), 305–321,
722 <https://doi.org/10.1029/JZ064i003p00305>, 1959.

723 Mendillo, M.: Storms in the ionosphere: patterns and processes for total electron content, *Rev. Geophys.*, 44 (4), RG4001,
724 <https://doi.org/10.1029/2005RG000193>, 2006.

725 Mosna, Z., Kouba, D., Knizova, P. K., Buresova, D., Chum, J., Sindelarova, T., Urbar, J., Boska, J., and Saxonbergova –
726 Jankovicova, D.: Ionospheric storm of September 2017 observed at ionospheric station Pruhonic, the Czech Republic, *Adv.*
727 *Space Res.*, 65 (1), 115–128, <https://doi.org/10.1016/j.asr.2019.09.024>, 2020.

728 Pirog, O. M., Polekh, N. M., Zherebtsov, G. A., Smirnov, V. F., Shi, J., and Wang, X.: Seasonal variations of the ionospheric
729 effects of geomagnetic storms at different latitudes of East Asia, *Adv. Space Res.*, 37 (5), 1075–1080,
730 <https://doi.org/10.1016/j.asr.2006.02.007>, 2006.

731 Polekh, N., Zolotukhina, N., Kurkin, V., Zherebtsov, G., Shi, J., Wang, G., and Wang, Z.: Dynamics of ionospheric
732 disturbances during the 17–19 March 2015 geomagnetic storm over East Asia, *Adv. Space Res.*, 60 (11), 2464–2476,
733 <https://doi.org/10.1016/j.asr.2017.09.030>, 2017.

734 Prölss, G. W.: Common Origin of Positive Ionospheric Storms at Middle Latitudes and the Geomagnetic Activity Effect at
735 Low Latitudes, *J. Geophys. Res.*, 98 (A4), 5981–5991, <https://doi.org/10.1029/92JA02777>, 1993a.

736 Prölss, G. W.: Ionospheric F-region storms. *Handbook of atmospheric electrodynamics 2*, 1st edition, edited by: Volland, H.,
737 CRC Press, Boca Raton, 195–248, <https://doi.org/10.1201/9780203713297>, 1995.

738 Prölss, G. W.: Ionospheric F-region storms: unsolved problems. In: *Characterizing the Ionosphere. Meeting Proc. RTO-MP-*
739 *IST-056. Paper 10. Neuilly-sur-Seine, France: RTO. 10–1 – 10–20. 2006.*

740 Prölss, G. W.: Magnetic storm associated perturbations of the upper atmosphere. In: *Magnetic storms*, edited by Tsurutani
741 B.T., Gonzalez W.D., Kamide Y., Arballo J.K., *Geoph. Monog. Series. Vol. 98. Washington, D.C.: AGU. P. 249–290. 1997.*
742 <https://doi.org/10.1029/GM098p0227>

743 Prölss, G. W.: On explaining the local time variation of ionospheric storm effects, *Ann. Geophys.*, 11 (1), 1–9, 1993b.

744 Shpynev, B. G., Zolotukhina, N. A., Polekh, N. M., Ratovsky, K. G., Chernigovskaya, M. A., Belinskaya, A. Yu., Stepanov,
745 A. E., Bychkov, V. V., Grigorieva, S. A., Panchenko, V. A., Korenkova, N. A., and Mielich, J.: The ionosphere response to
746 severe geomagnetic storm in March 2015 on the base of the data from Eurasian high-middle latitudes ionosonde chain, *J.*
747 *Atmos. Solar-Terr. Physics*, 180, 93–105, <https://doi.org/10.1016/j.jastp.2017.10.014>, 2018.

748 *Space Weather (Geophysical Monograph)*, edited by: Song, P., Singer, H., and Siscoe, G., Union, Washington, D.C.
749 <http://doi.org/10.1002/9781118668351>, 2001. ISBN 0-87590-984-1.

750 Vijaya Lekshmi, D., Balan, N., Tulasi Ram, S., and Liu, J. Y.: Statistics of geomagnetic storms and ionospheric storms at
751 low and mid latitudes in two solar cycles, *J. Geophys. Res.*, 116, A11328, <https://doi.org/10.1029/2011JA017042>, 2011.

752 Yakovchouk, O. S., Mursula, K., Holappa, L., Veselovsky, I. S., and Karinen, A.: Average properties of geomagnetic storms
753 in 1932–2009, *J. Geophys. Res.*, 117 (A3), <https://doi.org/10.1029/2011JA017093>, 2012.

754 Yamauchi, M., Sergienko, T., Enell, C.-F., Schillings, A., Slapak, R., Johnsen, M. G., Tjulin, A., and Nilsson, H.:
755 Ionospheric response observed by EISCAT during the 6–8 September 2017 space weather event: Overview, *Space Weather*,
756 16 (9), 1437–1450, <https://doi.org/10.1029/2018SW001937>, 2018.

757 Zalyubovsky, I., Chernogor, L., and Rozumenko V.: *The Earth–Atmosphere–Geospace System: Main Properties, Processes*
758 *and Phenomena, Space Research in Ukraine. 2006–2008. The Report Prepared by the Space Research Institute of NASU-*
759 *NSAU. Kyiv, 19–29, 2008.*

760 Zolotukhina, N. A., Kurkin, V. I., and Polekh N. M.: Ionospheric disturbances over East Asia during intense December
761 magnetic storms of 2006 and 2015: similarities and differences, *Solar-Terr. Physics*, 4 (3), 28–42,
762 https://ui.adsabs.harvard.edu/link_gateway/2018STP.....4c..28Z/doi:10.12737/stp-43201805, 2018.